2-14-2014

Examining Thin Film AlSb for Room Temperature Gamma Detectors

Erin Vaughan

Follow this and additional works at: https://digitalrepository.unm.edu/ne_etds

Recommended Citation

Erin Ivey Vaughan
_____

Candidate

Nuclear Engineering
_____

Department

This thesis is approved, and it is acceptable in quality and form for publication:

Approved by the Thesis Committee:

Adam Hecht, Chairperson
_____

Ganesh Balakrishnan
_____

Cassiano de Oliveira
_____

EXAMINING THIN FILM ALSB FOR ROOM TEMPERATURE GAMMA DETECTORS

by

ERIN IVEY VAUGHAN

B. A., ASTROPHYSICS, UNIVERSITY OF NEW MEXICO

THESIS

Submitted in Partial Fulfillment of the

Requirements for the Degree of

Master of Science

Nuclear Engineering

The University of New Mexico

Albuquerque, New Mexico

December, 2013

Acknowledgements

Without the guidance and positive reassurance of my advisor, Dr. Adam Hecht, and Dr. Ganesh Balakrishnan, this manuscript would never have been completed. Their continuous enthusiasm and encouragement were surely appreciated. I'd also like to thank Stephen Clark, Orlando Romero and Nassim Rahimi for their extensive contribution to the MBE growth and characterization chapters of this report.

My parents and siblings were especially helpful with their patience and gentle praise, always lifting my spirits during times of self-doubt. My mother, Susan Ivey, and step-father, Dean Reynolds, cheered me on from the audience as I nervously delivered my first presentation at a conference. In an act of considerable thoughtfulness, my father, Fred Husher, constructed (in his garage machine shop) experimental equipment for me to use in the lab when purchasing such a thing was beyond my budget.

Always keeping me focused, confident and determined is my husband, Jeremy. I can only hope he will be as supportive and persistent during my doctoral dissertation preparation.

Examining Thin Film AlSb for Room Temperature Gamma Detectors

by

Erin Ivey Vaughan

B. A., Astrophysics, University of New Mexico, 2006

M. S., Nuclear Engineering, University of New Mexico, 2013

Abstract

A thin film semiconductor device was grown by MBE methods, characterized for material quality and evaluated for suitability as a room temperature gamma radiation detector. The objective was to produce a device that was superior to current semiconductor detectors, namely HPGe and CZT which have different limitations due to intrinsic material characteristics. AlSb was chosen because of its desirable properties which include the high atomic number of antimony ($Z = 51$), relatively large band gap ($E_g = 1.6$ eV), and theorized high dual carrier mobility. Simulations were performed using MCNP5 to predict energy deposited in AlSb by low energy gammas from Ba-133 and Co-57. A benchmark model was developed using a silicon surface barrier detector to validate AlSb simulations. Prior to radiation experiments, a series of characterization methods were employed to evaluate the material quality. Surface features were measured by Nomarski imaging and AFM, revealing an orange peel texture and screw dislocations. The material composition was examined using XRD and the AlSb layer was observed to be fairly narrow

iv

along the lattice axis indicating reduced strain on the lattice structure. Electrical measurements were conducted which exposed low values for resistivity ($\rho = 10^{-3}$ Ω-cm) and average carrier mobility (~ 100 cm^2/Vs), and a high hole concentration ($\sim 10^{19}$ cm^{-3}). I-V curves indicated a leaky nature for the diode, and it is suspected that Zener breakdown was occurring.

During radiation experiments, no signal was observable above noise levels. The high hole concentration may have contributed to this result by eliminating the intended intrinsic region between the electrodes. Further studies should be conducted with AlSb to investigate the effects of compensation doping and/or growth temperature on carrier concentration and AlSb purity.

Table of Contents

List of Figures

ix

x

List of Tables

Chapter 1: Introduction

For gamma radiation, the most common detectors are sodium-iodide (NaI) scintillators, high-purity germanium (HPGe) semiconductors and cadmium-zinc-telluride (CZT) semiconductors.   For optimal resolution, HPGe detectors must be cooled to liquid nitrogen temperatures, limiting portability and ease of use.   NaI detectors are operable at room temperatures but are significantly inferior to HPGe with respect to energy resolution [3].   The most recent addition, CZT, operates at room temperature, has improved resolution [1] (compared to NaI), but has low hole mobility, reducing it to a single charge carrier detector.   A well-known disadvantage, the result is poor spectral performance [3], and reduced photopeak efficiency [1].   This also limits the detector thickness to maintain reasonable resolution, as an event near the cathode will have different charge collection properties than an event near the anode [3]. This effect will be revisited in detail in the following chapter.

New technology involving semiconductor production introduces new materials to be considered for use in this field.   The properties that impact the performance of semiconductor materials will be covered extensively in the following chapter.   Of the many compounds recently explored by various researchers, aluminum antimonide (AlSb) has several promising properties for radiation detection, some of which suggest that it may be operable at room temperature and maintain good resolution.   There are, however, several properties that remain unknown.   Until recently, only bulk growth methods had been used to produce AlSb and, due to difficulties with the material exposure to air and crucibles, high levels of defects were observed.   In spite of the encouraging theorized and measured characteristics [3], this reactivity has prevented production of AlSb by any method with low enough defect levels to achieve a gamma ray induced response measurable above noise.

The primary objective of this research was to examine the suitability and performance characteristics of AlSb as a radiation detector.   A discussion of the background and theory

1

surrounding the development of AlSb as a semiconductor detector is to follow in Chapter 2. Simulations using Monte Carlo methods were conducted and are covered in Chapter 3 and all relevant input files can be found in the appendix. AlSb sample material production and characterization measurements were performed and are described in Chapters 4 and 5, respectively, followed by a discussion of the results in Chapter 6. The radiation detection evaluation is described in Chapter 7, where experimental procedures and analysis is presented. Future work, discussed in Chapter 8, may be done to further determine the opportunities and restrictions involved with producing a radiation detector using AlSb.

Chapter 2: Background & Theory

2.1 Desirable Properties

When energetic photons interact with the semiconductor atoms, a large number of electron-hole pairs are generated proportional to the energy deposited by the incident photon. A reverse bias is applied to produce a depletion region so no current flows except for charge liberated by radiation in the depletion region itself. This depletion region is the active region of the detector. Due to the applied electric field the electrons and holes move as charge carriers through the semiconductor device toward the opposing electrodes. The charge induced on the electrodes varies according to the movement of the charge carriers and this charge is converted to a voltage pulse using a charge sensitive amplifier. The signal amplitude should be proportional to the energy deposited by the gamma radiation. [33]

The intrinsic or engineered crystal properties involving the generation and transit of electrons and holes are of considerable interest. These include the atomic numbers of the constituents, the band gap of the compound, and the charge induction efficiency (CIE).

2.1.1 Atomic Number, Z

The three types of photon interactions that are important for radiation detection measurements are photoelectric absorption, Compton scattering and pair production. The third mechanism only occurs when the incident photon energy exceeds 1.02 MeV (twice the electron rest mass), and remains highly improbable until photon energies reach several MeV [8]. This work is more confined to the sub-MeV region where photoelectric and Compton effects are relevant.

Semiconductor compounds with large atomic number Z exhibit a high interaction cross-section for energetic photons. As the atomic number increases, the likelihood of photoelectric effect interactions occurring at higher incident photon energies also increases, expanding the range over which full photon energies are absorbed, thus improving the peak efficiency. The photoelectric effect dominates photon interactions below a few hundred keV, and that effect is strongly dependent on the atomic number of the material. Above that energy, Compton scattering is less strongly dependent on, but scales linearly with, Z.

During photoelectric effect interactions all of the photon energy is absorbed in the collision. An inner shell electron is then ejected, called a photoelectron, from the atom with a kinetic energy equal to the difference between the incident photon energy ($h\nu$) and the electron binding energy (E_1), $E=h\nu-E_1$. Then, an outer shell electron moves to fill the vacancy, resulting in the emission of characteristic x-rays which are also typically absorbed in the material. The absorption cross section for photoelectric effect photons is:

$$\substack{a\\p}\sigma = AZ^n(h\nu)^{-s} \tag{1}$$

where A is constant, $4<n<5$ and $1<s<3.5$ [29]. The mass attenuation plot in Figure 1 illustrates how the cross section for the photoelectric effect (PE) decreases with increasing incident photon energy for AlSb ($Z_{Sb}=51$, $Z_{Al}=13$) and Ge (Z=32), and is a trend with all materials. The log-log representation of the plot is shown to illustrate large-scale features but it should be noted that the interaction cross section is 10,000 times larger for 1 keV photons than for 100 keV photons.
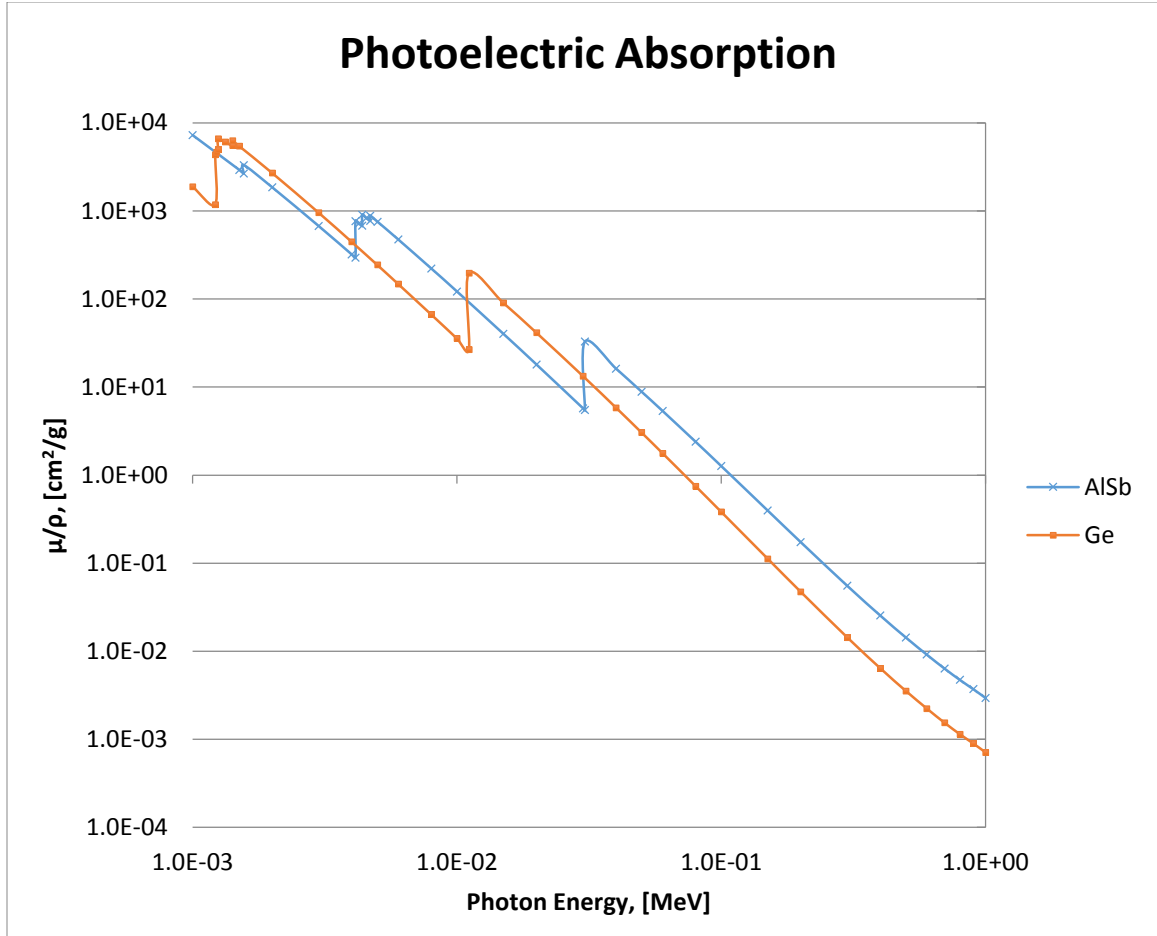
Figure 1.   Mass attenuation curves for AlSb and Ge. [2]

A Compton scattering interaction occurs when an incident photon collides with a stationary electron, transferring a portion of its energy.   The energy transferred is dependent on the scattering angle and can range from zero to a large fraction of the gamma ray energy.   If zero energy is transferred the photon retains its initial energy (hν) and simply scatters with a scattering angle of zero degrees, according to equation 2, where hν' is the scattered photon energy. [8]

$$hv' = \frac{hv}{1 + \frac{hv}{m_0 c^2}(1 - cos\theta)} \tag{2}$$

5

The scattered photon can then be reabsorbed by photoelectric effect resulting in a full energy deposition.

An atomic number greater than 40 is said to be competitive with germanium without requiring excessive detector thickness [29].

2.1.2 Band Gap

The energy difference between the conduction band and the valence band, commonly referred to as the band gap, determines the energy required to ionize atoms within the crystal.   A smaller band gap means a greater number of charge carriers (N) are released per energy deposited and, due to higher statistics and lower proportional variation, higher resolution.   From Poisson statistics, the relationship to the device resolution (from the standard deviation, $\sigma = (E_\gamma/\varepsilon)^{1/2}$) goes approximately as $N^{1/2}$, or $\varepsilon^{-1/2}$, where ε represents the energy required to form an electron-hole pair.

The probability of thermal ionization is also large, so narrow band gap detectors must be operated at very low temperatures for optimal performance.   The number of thermal carriers generated is proportional to $\exp(-E_g/k_BT)$, where E_g is the band gap energy, k_B is the Boltzmann constant, and T is absolute temperature.   Increased E_g allows for increased T.   If the band gap is larger, dopants (which are used to provide steps across the band gap) can be used to accurately adjust the physical properties of the semiconductor to suit the targeted energy detection range.

For room temperature operation with intrinsic detector noise reduced to an acceptable level, a band gap between about 1.4 and 2.2 eV is imperative.   The lower limit reflects the minimization of the background signal from thermally generated carriers, while the upper limit represents a maximization of the number of carriers generated as a result of radiation energy deposited. [16]

The distribution of electrons in a semiconductor device is governed by the Fermi function, equation 3 below, and is illustrated by the diagrams in figure 2.

6

$$f(E) = \frac{1}{1 + \exp\left(\frac{E - E_F}{k_B T}\right)}$$

(3)
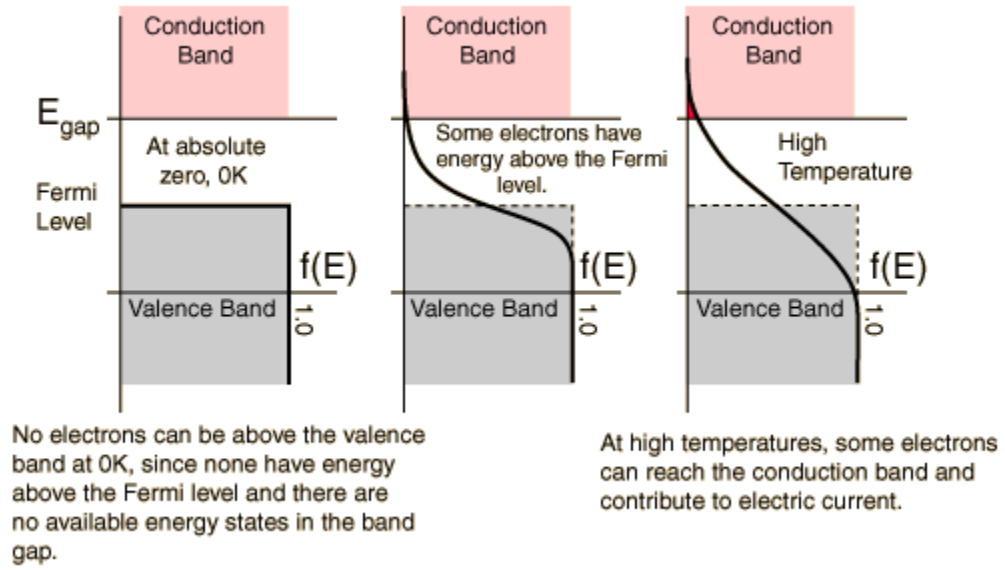
Figure 2.   Fermi-Dirac distribution with increasing temperature [43]

The number of available states, or the density of states (ρ) is given in equation 4 as a function of energy.   The product of the density of states and the probability of occupation of those states gives the number of electrons per volume with energy between E and dE.

$$\rho(E) = \frac{8\sqrt{2}\pi m^{3/2}}{h^3} \sqrt{E - E_{gap}}$$

(4)

$$N(E)dE = \rho(E)f(E)dE = \frac{8\sqrt{2}\pi m^{3/2}}{h^3} \sqrt{E - E_{gap}} \frac{1}{e^{(E-E_F)/kT} + 1} dE$$

(5)

$$where \quad E_F = \frac{E_{gap}}{2}$$

7

As equation 6 shows, the electron population in the conduction band, N_{cb}, can be calculated by integrating this product from the top of the band gap to infinity. [42]

$$N_{cb} = \int_{E_{gap}}^{\infty} N(E)dE = AT^{3/2}e^{-E_{gap}/2kT}$$

(6)

$$where \ A = \frac{8\sqrt{2}(\pi mk)^{3/2}}{h^3} = 4.83 \times 10^{21} \frac{electrons}{m^3 K^{3/2}}$$

The number of thermally generated electrons were calculated for relevant band gap energies and temperatures, shown in table 1. Values for HPGe are given for liquid nitrogen and room temperatures. Notice that fewer thermal electrons are generated for AlSb than for CZT.

Table 1. *Number of electrons in the conduction band for HPGe cooled to liquid nitrogen temperatures, CZT and AlSb at room temperature, and the upper and lower limits for desirable band gap for semiconductor radiation detectors*

Semiconductor	E_{gap} [eV]	@ T [K]	Number of Electrons in Conduction Band [electrons/ m^3]
HPGe	0.74	77	1.98
HPGe	0.74	300	1.53×10^{19}
Lower Limit	1.4	300	4.36×10^{13}
CZT	1.57	300	1.63×10^{12}
AlSb	1.6	300	9.11×10^{11}
Upper Limit	2.2	300	8.31×10^{6}

Figure 3 illustrates the effect of a reverse bias on a semiconductor with a P-I-N junction [44]. Placed between the p+ and n+ doped regions, the "I" region is ideally intrinsically semi-insulating and provides for a constant electric field through a large depletion zone. This allows for the consistent proportionality of the output signal to the energy deposited by incident radiation interactions.

8
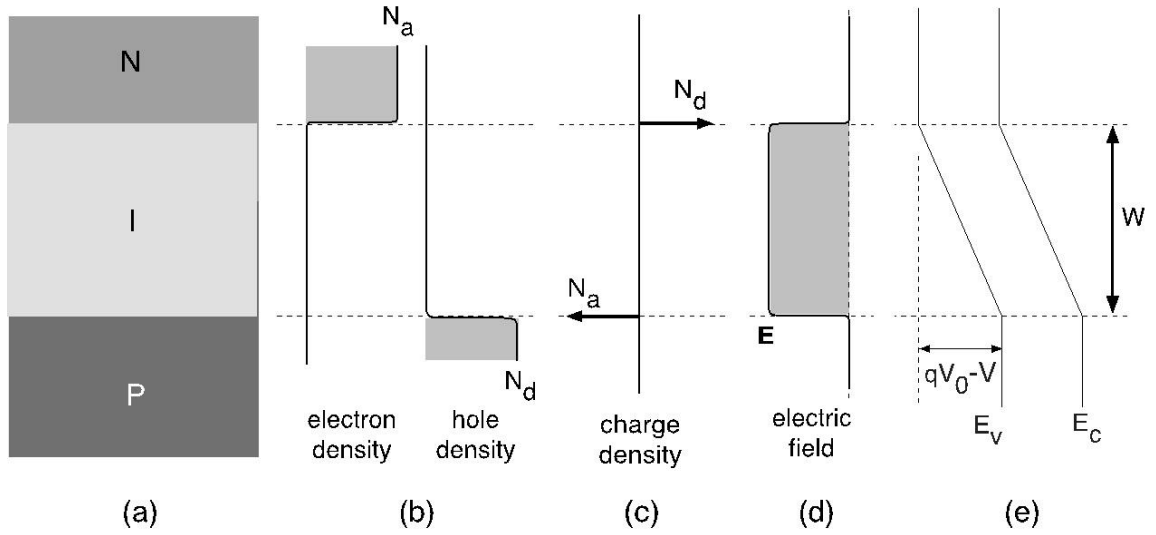
Figure 3. Diagrams showing the (a) structure, (b) carrier distribution, (c) charge distribution, (d) electric field, and (e) energy bands of a P-I-N diode under reverse bias [44]

2.1.3 Charge Transport

The transport of charge carriers in semiconductor materials is a crucial intrinsic parameter, which can be evaluated by observing the drifting behavior of electrons and holes under an applied bias voltage.   For optimal signal generation, a quantity known as charge induction efficiency (CIE) is maximized.   Simply, CIE is a ratio of the measured induced charge on an electrode (Q_m) to the charge actually created in the material (eN), CIE = Q_m/eN.   For perfect charge induction this ratio is 1, meaning the all of the holes and electrons are fully accounted for at the electrodes.   In reality, impurities and defects trap charge carriers so that perfect CIE is never achieved. [3]

The product of charge mobility (μ) and carrier lifetime (τ) is of particular interest for calculating the induction efficiency, η.

$$\eta(x) = \frac{(\mu\tau)_e E}{D}\left[1 - \exp\left(-\frac{D-x}{(\mu\tau)_e E}\right)\right] \;+\; \frac{(\mu\tau)_h E}{D}\left[1 - \exp\left(-\frac{x}{(\mu\tau)_h E}\right)\right] \qquad (7)$$

9

Here, D is the detector thickness, E is the electric field intensity (E=bias voltage/detector thickness for planar geometry), x is the distance from the cathode, and $(\mu\tau)_e$ and $(\mu\tau)_h$ are mobility-lifetime products for electrons and holes, respectively.   Called Hecht's Relation [8], it describes the behavior of charge transport, as a function of the distance (x) from the cathode surface, that the radiation interacted and separated the charges.   If η is non-uniform the spectral resolution of the detector will be compromised.
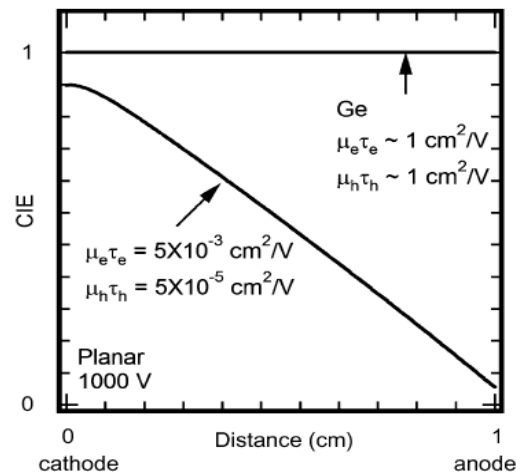
Figure 4.   Charge induction efficiency [3]

As is depicted in figure 4, germanium maintains constant CIE regardless of a carrier's distance from the electrodes.   This is a result of germanium's symmetric and high $\mu\tau$ properties for electrons and holes, allowing for consistent charge collection.   The angled line in figure 4 represents typical values for electron and hole $\mu\tau$ products for CZT.   CZT has low hole mobility and poor hole lifetime properties (compared to HPGe) which causes lower CIE for radiation interactions near the anode, following Hecht's equation.   This can be interpreted as holes moving slowly towards the cathode and the induced pulse thus being broad and being lost to shorter amplifier shaping times, a ballistic defect.   On top of that, defects and crystal impurities can trap charges on their path.   The result is a low energy tail, meaning poorer photo-peak efficiency within the 12-14% energy window around the

10

photo-peak of interest [1].   This is illustrated for Tc-99m, a common isotope used in nuclear medicine, in Figure 5, where the curve shaded in yellow represents the spectrum expected from CZT and the curve without shading is indicative of a NaI spectrum.
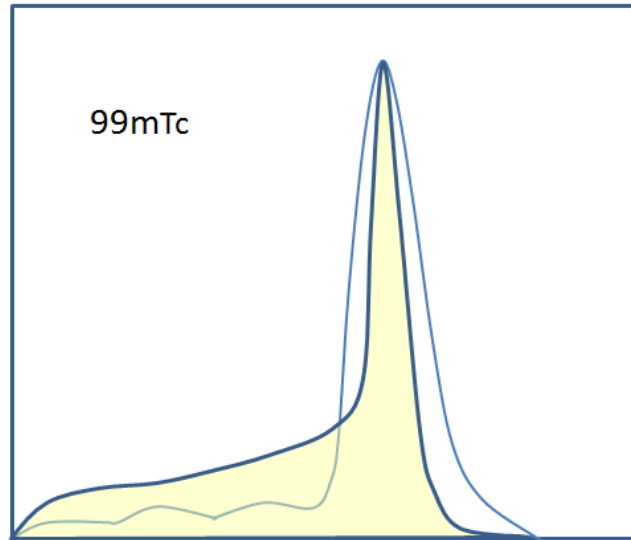
Figure 5.   Tc-99m 140 keV spectra obtained with CZT (shaded in yellow) and NaI (light blue outline). Notice the low-energy tailing of the CZT.   [1]

High counting statistics requires high carrier mobilities and long carrier lifetimes.   An indirect band gap can improve carrier lifetimes by quenching radiative recombination [15]. At room temperature the mobility, μ, will be limited by electron-phonon scattering, although defects in the material can cause μ to be considerably lower.

A higher carrier mobility (μ) and longer lifetime (τ) means improved charge detection.   A $\mu\tau$ product greater than about 0.1 cm^2/V is preferred for optimal detector resolution. [16]

2.2 Current Popular Semiconductor detectors

The table below outlines several emerging or recently improved compound semiconductor

11

materials that have been evaluated for desirable radiation detection properties. Germanium is also included for comparison. Based on these values, it's easy to compare performance characteristics such as the peak efficiency (atomic number), room temperature operation (band gap) and consistent resolution across the energy spectrum (carrier lifetime and mobility).

Table 2.   Useful material properties for some semiconductor radiation detectors [3].

Material	Ge (77K)	HgI$_2$	CdTe	CdZnTe	GaAs	AlSb
Atomic number	32	80, 53	48, 52	48, 30, 52	31, 33	13, 51
Band gap (eV)	0.74	2.13	1.50	1.57	1.43	1.6
Energy per e-h pair (eV)	2.97	4.2	4.4	4.6	4.2	?
Fano factor	0.08	0.19	0.11	0.09	0.14	?
μ_e (cm^2/Vs)	40,000	100	1100	1000	8000	1100
μ_h (cm^2/Vs)	40,000	4	100	10	400	700
τ_e (s)	10^{-3}	10^{-6}	10^{-6}	10^{-6}	10^{-8}	?
τ_h (s)	10^{-3}	10^{-5}	10^{-6}	10^{-6}	10^{-7}	?

With the exception of liquid nitrogen cooled Ge and AlSb, all of the compounds summarized above have highly non-symmetric values for electron and hole mobilities, which suggests inferior spectral performance. While Luke et al. [3] and Lordi et al. [16] report relatively large theorized mobilities for AlSb (μ_e = 1100 cm^2/Vs and μ_h = 700 cm^2/Vs), other researchers [22, 25] present much smaller measured values (μ_e = 60 to 200 cm^2/Vs and μ_h = 100 to 400 cm^2/Vs). As was mentioned previously, there are several properties that have not been reported for AlSb. However, the large atomic number for antimony (Z=51) and the size of the band gap (1.6 eV) are well-established values, and are encouraging for the purpose of this study.

Chapter 3: Simulations & Benchmarking

Monte Carlo simulations were performed using floating object in vacuum geometry. To benchmark the simulation work, models were developed for a silicon surface barrier (SSB) used as a thin film x/gamma-ray detector, exposed to Ba-133 and Co-57 x/gamma-rays, and the results were compared to measured spectra. Simulated spectra for Ba-133 and Co-57 were broadened using MCNP Gaussian techniques to more closely approximate measured spectra.

3.1 Benchmarking

To benchmark simulations for AlSb detector behavior, modeling of a SSB detector response was compared with measurements. Simulations were conducted using MCNP version 5 with photon data from the ENDF/B-VI.8 library [7]. Co-57 and Ba-133 were selected for experimental measurements for their low energy photons. This is important for thin samples where low energy photons have reasonable interaction efficiency. Because the materials were grown by MBE methods, the AlSb layer thickness was limited to 5 microns. To keep the dimensions as similar as possible, the thinnest (50 microns) SSB detector available in the lab was chosen for benchmark experiments.

The SSB detector geometry was modeled with a gold contact layer 1 micron thick and the isotropic point source was placed 1.5 mm away, as the images generated by MCNP5 in figure 5 illustrate. The medium between the source and the detector is air (0.755636% N, 0.231475% O, and 0.012889% Ar, by weight) with a density of 0.0013 g/cm^3, depicted in yellow. In the image on the right side of figure 6 the silicon and gold layers can be seen. The vertical lines represent boundaries for geometry splitting variance reduction.
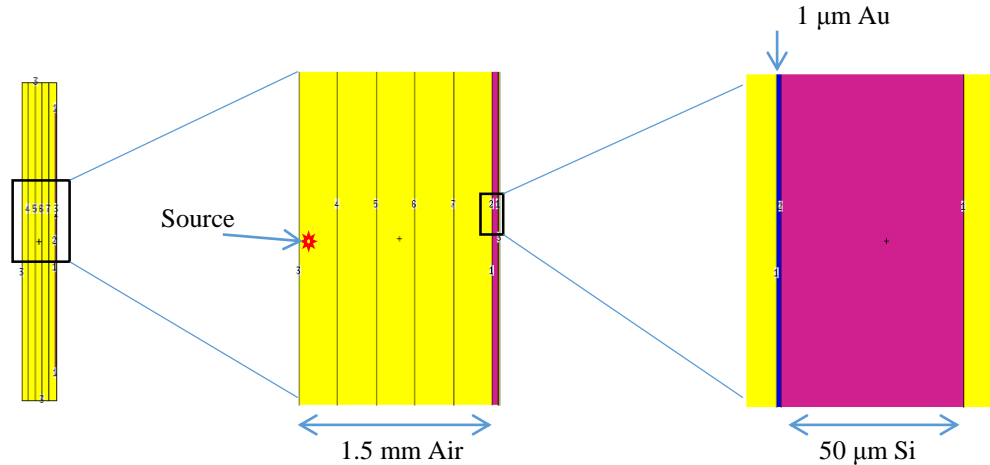
Figure 6.   SSB detector geometry as modeled with MCNP5

To determine the number of photons needed for acceptable statistics, an F4 mesh tally was applied.   Figure 7 depicts the particle flux and relative error for 100,000 (two left images) and 10,000,000 photons (four right images) generated by MCNP5.   The mnemonic "nps" is the terminology used in the MCNP User's Manual [6] to represent the number of histories to be tracked during a single execution.   The relative error color scale is also shown at the bottom right of figure 7, with purple representing 100% and orange representing 0% uncertainties.   The two left images in figure 7 show the side view of the SSB detector volume with boundaries corresponding to those shown in figure 6.   Shown are the photon flux (far left), most concentrated in red where the source is closest to the detector, and associated relative error (center left) where a statistical uncertainty of greater than 25% is observed over much of the region.   Similarly, the images on the top right of figure 7 represent a top view (analogous to figure 6) of the particle flux in the detector where the source is centered (center right) and associated relative error (far right) with most relative errors below 5%.   Side views and relative errors of this same detector are shown in the lower images, (center right and far right, respectively).   To reduce statistical variation to less than 5%, 10,000,000 photons were tracked for each simulation.

14

nps 100,000   nps 10,000,000

Primarily greater
than 25%
relative error

1
.5
.25
.15
.1
.05
0

Primarily
less than
5% relative
error
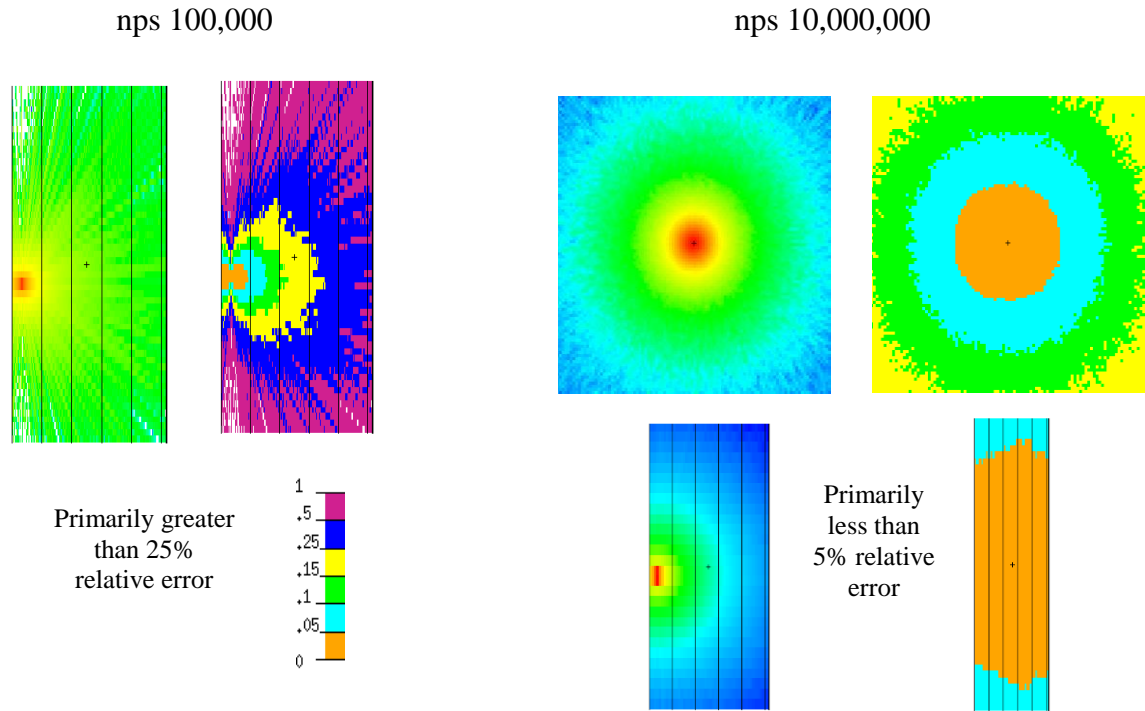
Figure 7.   F4 mesh tally showing particle flux and associated relative error.   Particle fluxes are shown with highest and lowest intensity indicated by red and blue, respectively.   The relative error scale is shown (bottom left) ranging from 0 (0%) to 1 (100%).

3.2 AlSb Simulation Model

For reasons that will be discussed thoroughly in Chapter 4, the geometry for the AlSb structure is more complicated, making modeling of the AlSb detector slightly more challenging.   In addition to the 5 micron thick AlSb layer, the structure design includes 0.1 microns GaSb to provide strain relief between mismatched AlSb and GaAs lattices, a 300 micron thick GaAs substrate, another GaSb layer to prevent exposure of the AlSb to oxygen, and ohmic contact layers on each side.   The structure is shown in figure 8 (left), where layer thicknesses are not represented to scale.

15

Structure

Simulated Geometry

25 nm Ti, 25 nm Pl, 50 nm

100 nm GaSb p+

5 µm AlSb

100 nm GaSb

GaAs substrate,

25 nm Ge, 54 nm Au, 5 nm Ni, 200 nm

AlSb Layer
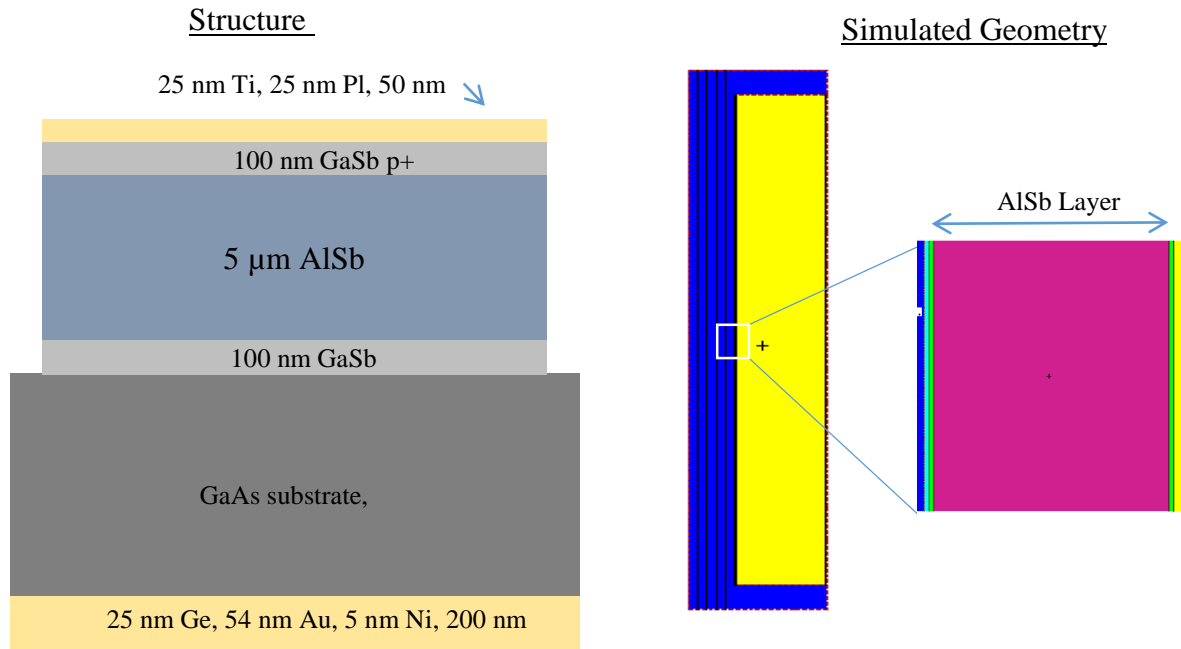
Figure 8.   AlSb growth structure design (left) and MCNP5 simulation geometry (right)

To simplify things very slightly the ohmic contact layers were modeled using Au exclusively, neglecting the other elemental components but maintaining the overall layer thickness.   Geometry splitting was used as a variation reduction technique in the air region between the source and the detector surface.   The simulated geometry, generated by MCNP5, for AlSb is shown in figure 8 (right), where the scale is accurate.   The dark blue region in this case depicts air and yellow is the GaAs substrate.   The image on the far right shows the AlSb layer (purple) and the other nearby layers.

Again, a mesh was used to confirm that the number of particle histories tracked is statistically appropriate, illustrated in figure 9.   The images show the photon flux (top) and associated relative error (bottom) for side and top views of the AlSb detector for 100,000 and 10,000,000 particle histories.   The black rectangular line in each side view represents the outermost detector structure boundary.

16

nps 100,000   nps 10,000,000
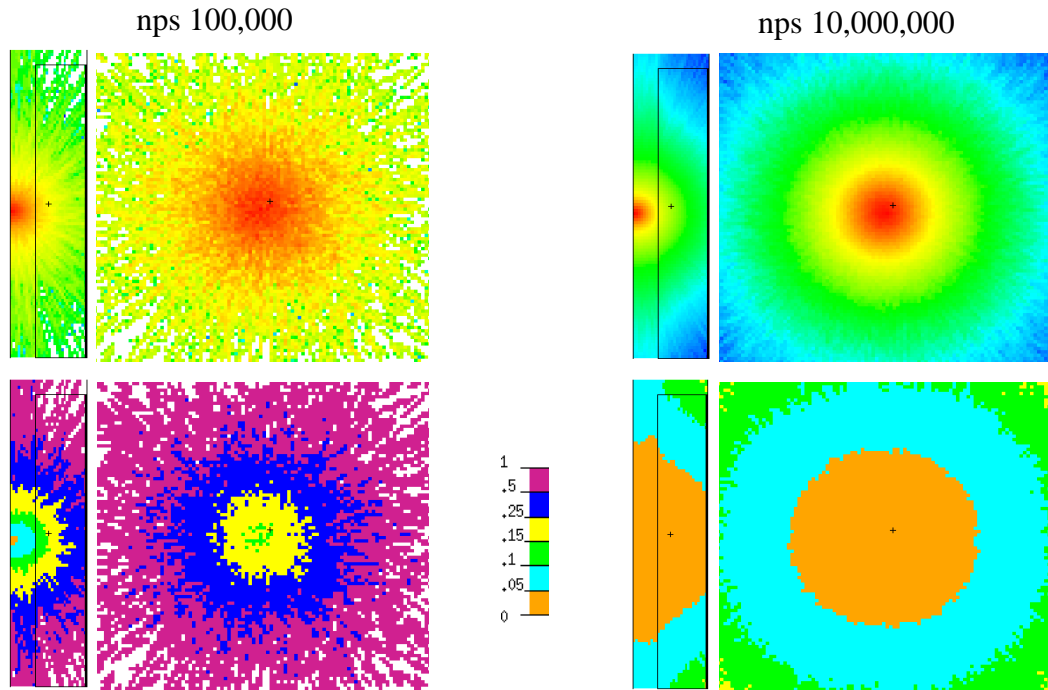
Figure 9.   Photon flux and associated relative error for MCNP5 simulation of AlSb detector, where each set of images shows the top and side views of the detector.   The right and left columns of images correspond to 100,000 and 10,000,000 simulated particle histories, respectively.   Particle fluxes (top row) are shown with highest and lowest intensity indicated by red and blue, respectively.   On the bottom are the associated relative error results for each simulation.   The relative error scale is shown (bottom center) ranging from 0 (0%) to 1 (100%).

The SSB detector response was simulated using an F8 pulse height tally for modeling spectra from Co-57 and Ba-133.   An attempt was made to modify the spectra with the Gaussian energy broadening function in MCNP5.   Because of the thin film nature of the material being modeled, the thick-target bremsstrahlung approximation was removed from the physics of the problem by setting IDES=1.   All of the MCNP5 input files are included in the appendix at the end of this document.

The SSB simulations were compared with measurements for benchmarking.   These are compared graphically in figures 10 (Co-57) and 11 (Ba-133).   The measurements were performed with Co-57 and Ba-133 sealed sources and a 50 micron thick SSB detector in a light tight metal box with an Ortec 142 preamp and Ortec 428 bias supply.   Pulse height data were digitized using an Ortec Easy-MCA module.   The linear, semi-log and

17

broadened plots on the left sides of figures 10 and 11 were produced using the MCNP plotter. On the right side, spectra from actual measured counts are shown.
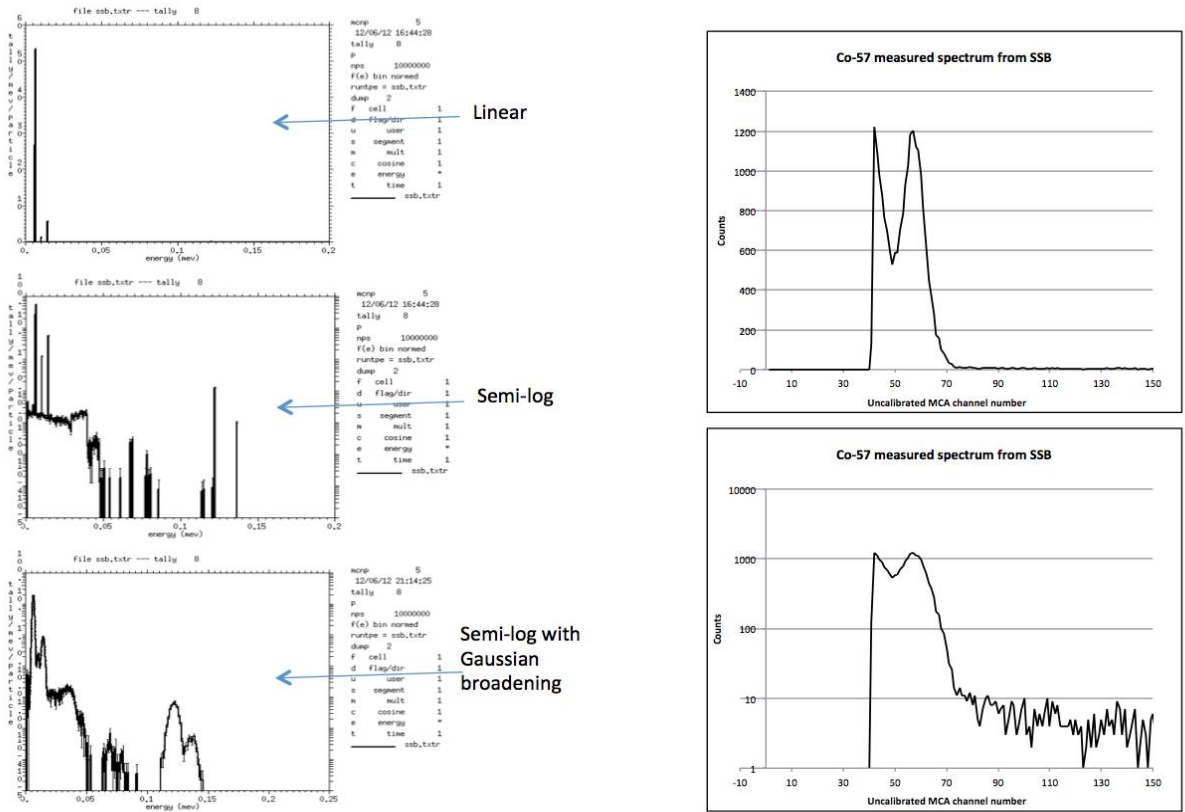
Figure 10.   Simulated (left) and measured (right) Co-57 spectra for SSB detector

The absence of measured data between channel numbers 0 and 45 was a deliberate low energy cut off, performed to isolate peak features in the spectrum from low pulse height electronic noise.   Some features in the measured semi-log plots may correspond to features in the simulated semi-log Gaussian broadened plots.

18
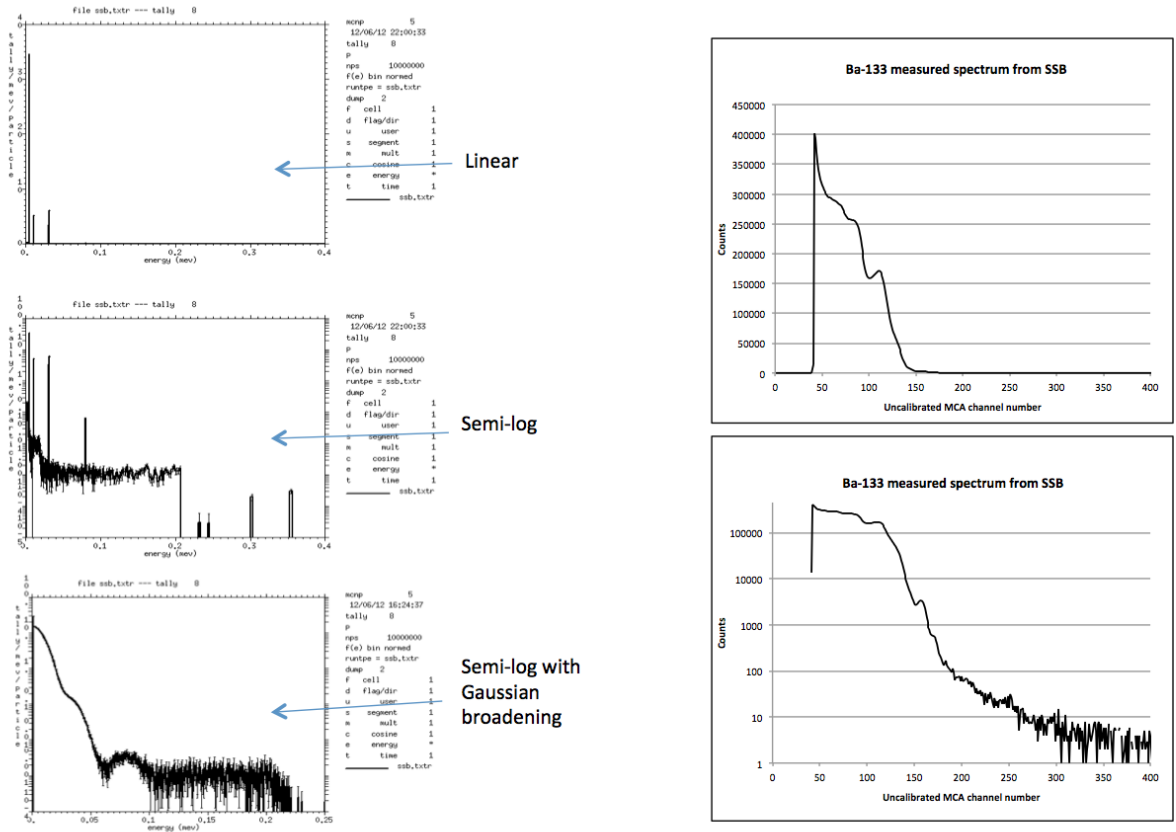
Ba-133

Figure 11.   Simulated (left) and measured (right) Ba-133 spectra for SSB detector

MCNP5 requires three known FWHMs to calculate the values used by the Gaussian energy broadening (GEB) function to modify the simulated spectra [6].   The measured spectra from the SSB detector did not generate resolution sufficient to calibrate the MCA. Therefore, a FWHM was not measured and could not assist in simulating peak broadening. Instead, a series of reasonable guesses were made to produce the broadened spectra shown.

Figures 12 (Co-57) and 13 (Ba-133) portray the simulated spectra (without broadening) for the AlSb detector on the left, compared to the SSB detector on the right.

19

Co-57

Simulated AlSb
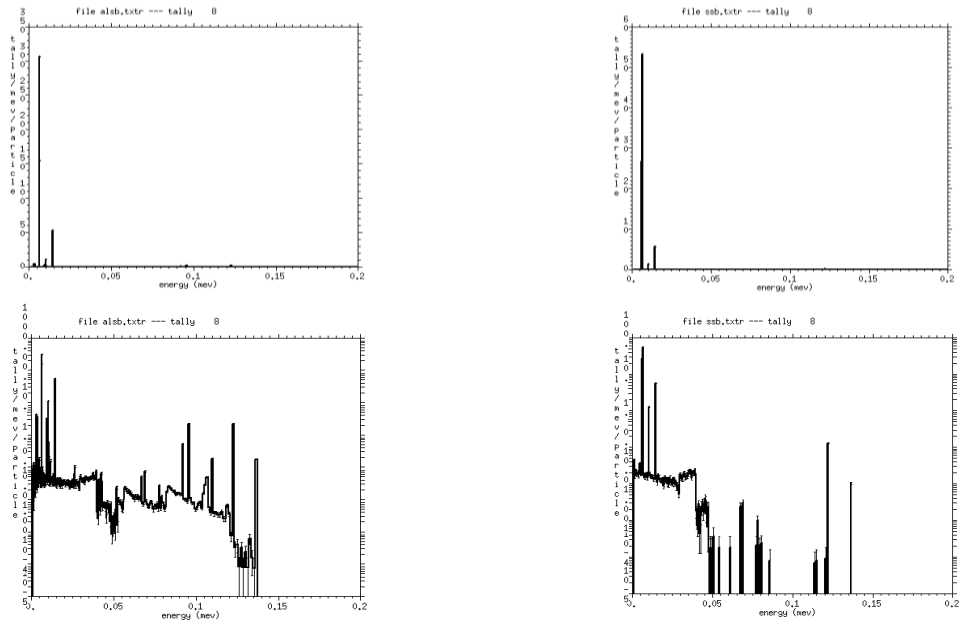
Simulated SSB

Figure 12. Simulated linear (top) and semi-log (bottom) spectra for AlSb (left) compared to SSB (right) for Co-57

Ba-133

Simulated AlSb
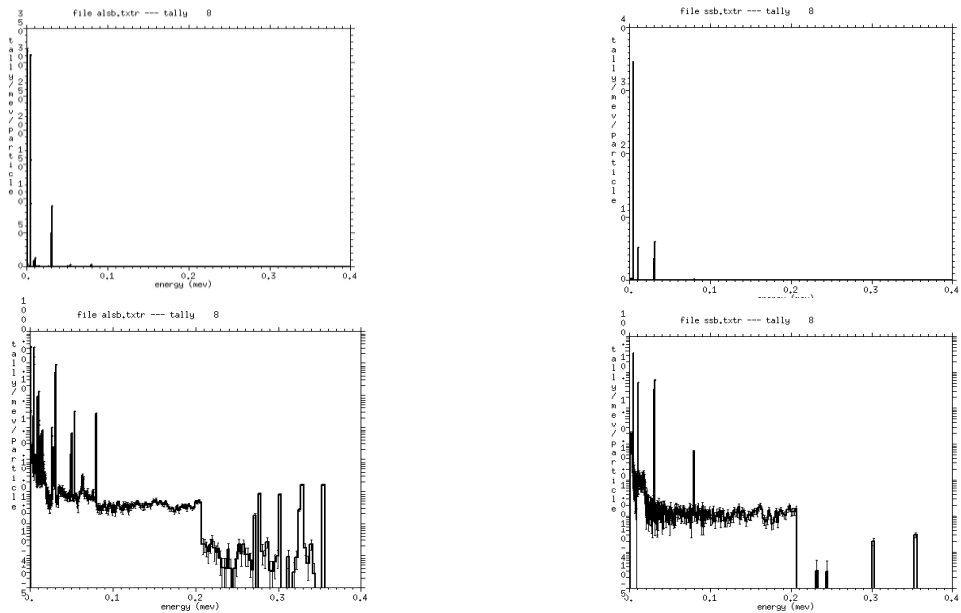
Simulated SSB

Figure 13. Simulated linear (top) and semi-log (bottom) spectra for AlSb (left) compared to SSB (right) for Ba-133

For Co-57 the number of simulated counts in the highest energy peak, $E_{x\text{-}ray}$=6.4 keV, was 310 for AlSb and 54 for SSB, as seen in figure 12. In the case of Ba-133, shown in figure 13, the photon count was 310 and 34 for AlSb and SSB, respectively, for the highest peak associated with x-rays having energy equal to about 4.4 keV. The semi-log simulated plots for both radioisotopes reveal improved details and structure with AlSb when compared to SSB. Simulated AlSb spectra include more counts overall, with about 10 times more photons being detected across the energy spectrum, and much higher efficiency at higher energies for these thin films, even with a thinner AlSb than SSB. This apparent improved detection efficiency can be attributed to the higher atomic number of AlSb (Z_{Sb} = 51) compared to Si (Z = 14).

Geometry splitting is not a recommended method of variance reduction for F8 tallies [6]. Instead, the weight windows method is suggested for most accurate results, although use of the weight windows generator is discouraged. Modifying the variance reduction technique could be addressed in future work.

In spite of difficulties involving variance reduction and GEB functions, simulated spectra were generated with features comparable to measured SSB spectra for both Co-57 and Ba-133. Based on this observation, the simulated AlSb spectra suggests that more photons overall should be detected with thin film AlSb, and that known energy peaks should be identifiable.

Chapter 4:   Sample Production

Traditionally, detector crystals are grown by bulk methods, which is very effective for producing large, unreactive materials. Because gamma rays can have long interaction lengths, bulk materials increase detection efficiency for higher energy photons.   While it has been attempted, AlSb production by bulk methods is quite difficult and results in high defect crystals.   This is due to the high reactivity of both Aluminum and antimony to air, and the extremely volatile reactivity of molten AlSb with all types of crucibles [11].

4.1 Growth by Heteroepitaxy

Molecular beam epitaxy (MBE) is a material growth technique that utilizes one or several molecular beams to deposit a series of single atomic layers, or monolayers, onto a heated crystalline substrate.   Solid materials are kept in evaporation cells which may be opened or closed depending on the atom or compound being deposited.   The temperature of the substrate is adjusted according to the desired surface structure.
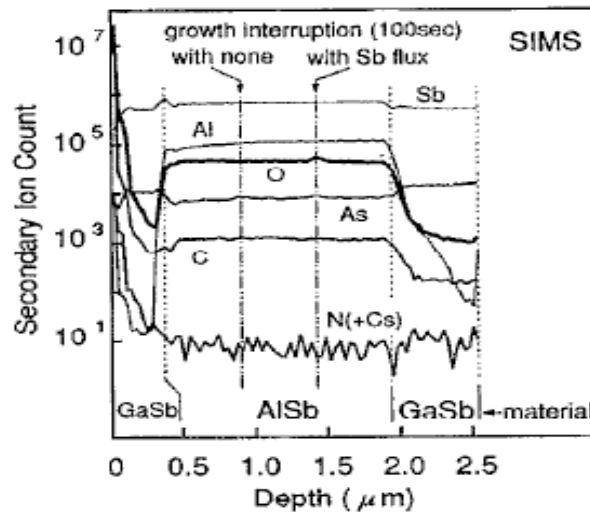
Figure 14.   SIMS profile of MBE grown AlSb [4]

22

Previous AlSb research was conducted using MBE methods nearly 20 years ago in 1994. Secondary Ion Mass Spectrometry (SIMS) results are illustrated in figure 14, which shows high oxygen content in the AlSb layer originating from oxygen incorporated during growth from the Sb source material [4].

Recent improvements in antimony purity, minimizing exposure to air during chamber loading, and more effective out-gassing techniques reduce deep level defects in AlSb associated with oxygen. These developments allow for production of an AlSb crystal that is nearly defect free and potentially detector grade. Introducing sophisticated growth techniques [13], collaborators at the Center for High Technology Materials (CHTM) at the University of New Mexico were able to produce several AlSb crystals by MBE for use in this research. The MBE growth chamber at CHTM is pictured in figure 15.
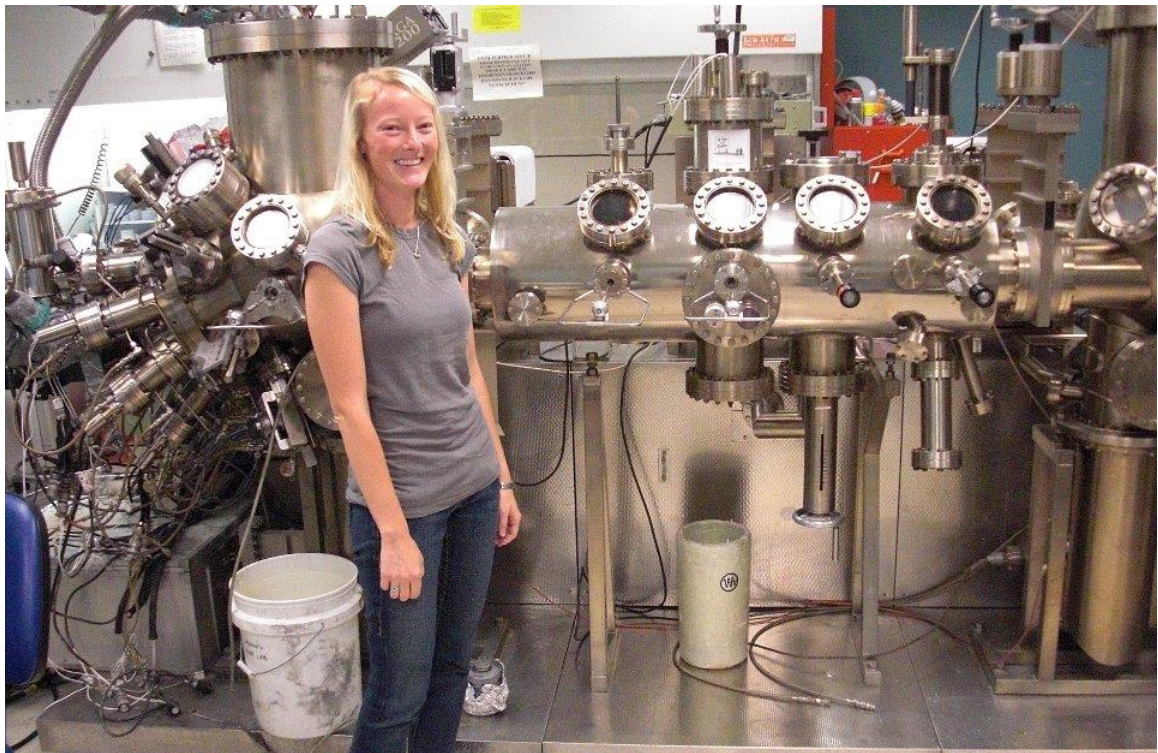
Figure 15.   MBE growth chamber at CHTM

4.2 Growth Structure

For the substrate material, GaAs is used exclusively in this study due to its relatively low cost and ability to be removed by etching, if desired.   This introduces, however, a large lattice mismatch between the substrate and the AlSb epi-layer.   The strain related defect density, which includes misfit and threading dislocations, grows quickly with increasing lattice mismatch between epi-layers [5].
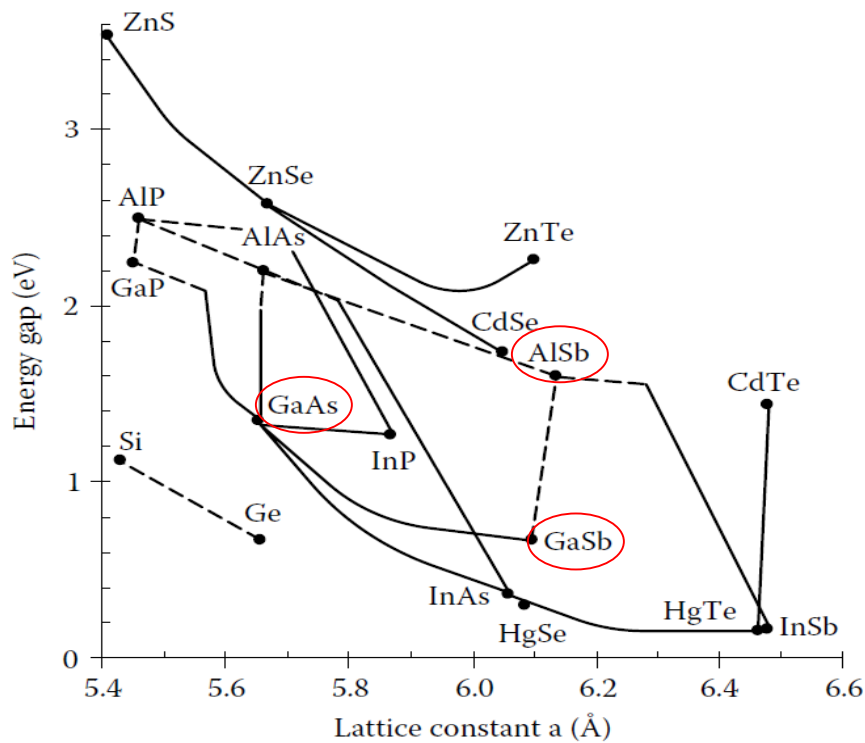
Figure 16.   Lattice constants and bandgap energies for III-V semiconductors at room temperature.   Dashed lines indicate an indirect gap. [5]

The diagram in figure 16 shows the distribution of lattice constants for many semiconductor compounds while the compounds of interest for this study are circled. From this diagram it is easy to recognize compounds that have similar lattice parameters and might be more compatible as sequential epitaxial layers during MBE growth. The

strain introduced by the lattice mismatch is simply:

$$f \equiv \frac{a_s - a_e}{a_e} \quad [\%] \tag{8}$$

where a_s and a_e are the lattice constants of the substrate and the epilayer, respectively. Using the lattice values in table 3, below, and equation 8, the magnitude of the strain can be calculated for each epitaxial layer. For AlSb grown directly on the GaAs substrate, a mismatch of 8.53% would introduce large strain leading to high threading dislocation densities.

Table 3.   Lattice constants for important AlSb diode structure layer interfaces [5]

Compound	Lattice Constant, *a* [Å]
GaAs	5.6534
GaSb	6.0960
AlSb	6.1357

Using the Matthews and Blakeslee Force Balance Model, as is derived by Ayers [5], the thickness of an epitaxial layer of a non-homogenous structure is limited due to strain caused by mismatched lattice constants. Termed the Critical Layer Thickness, h_c can be calculated using equation 9 below.

$$h_c = \frac{b(1 - v\cos^2\alpha)[\ln\left(\frac{h_c}{b}\right) + 1]}{8\pi|f|(1 + v)\cos\lambda} \tag{9}$$

25

For (001) zinc blende semiconductors, $\cos\alpha = \cos\lambda = 1/2$, $b = a/\sqrt{2}$, and $v \approx 1/3$. If a layer thickness is less than the critical thickness, $h < h_c$, the strain force will not overcome the tension between atoms in the layer. However, if the critical thickness is exceeded, $h > h_c$, lattice relaxation will occur and threading dislocations will become misfit dislocations at the epilayer interface. [5]
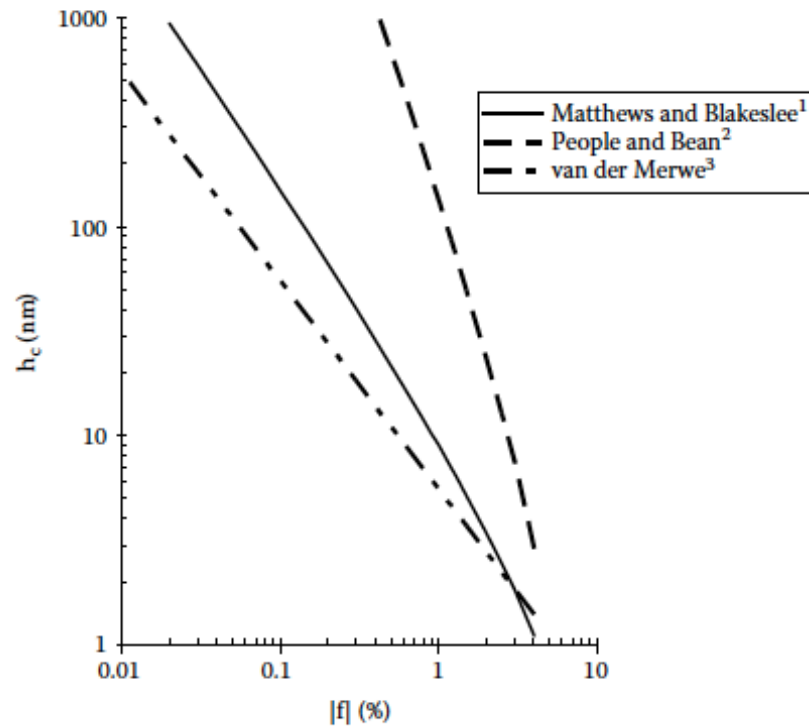
Figure 17.   Critical layer thickness as a function of lattice mismatch [5].

The relationship between the critical layer thickness, as derived by Matthews and Blakeslee, People and Bean, and van der Merwe, is shown in figure 17 above [5].

There are three stages that occur during the epitaxial growth process.   The initial stage is the pseudomorphic stage, which exists when the thickness is less than the critical thickness. The strain at this point is 100%.   When the growth exceeds the critical thickness dislocations begin to occur in the material.   This reduces the strain and the material is said

26

to relax.   To overcome this limiting factor, and ultimately to decrease threading dislocations propagating all the way through the structure, an interfacial misfit (IFM) dislocation layer is employed using GaSb.   The following images [34] in figure 18 illustrate the formation of IFM dislocations, which would allow for strain relief between the GaSb and GaAs layers, and provide a closer lattice matched surface for subsequent AlSb growth.   Using equation 8, the mismatch between GaSb and AlSb is only 0.65%.
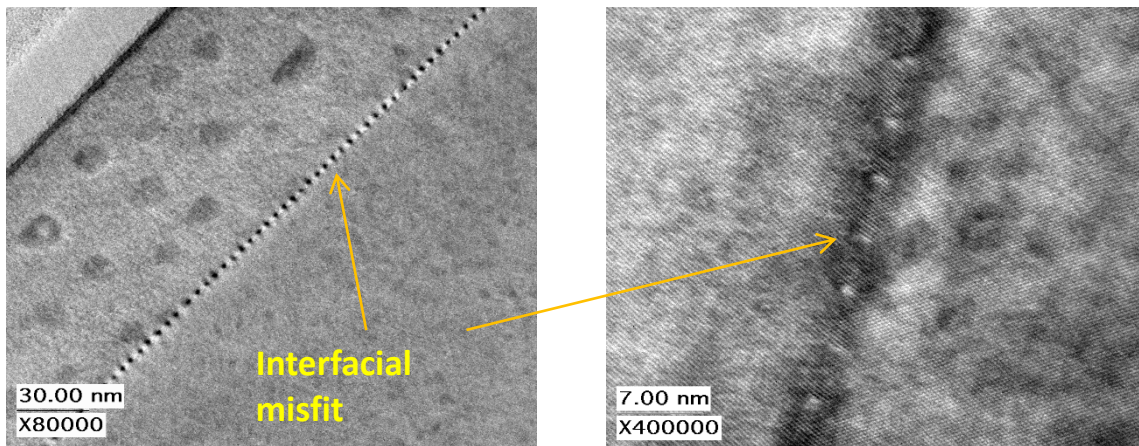
Figure 18.   IFM dislocations allowing for strain relief between GaSb epi-layer and GaAs substrate

Ultimately, the thickness of the AlSb epi-layer is limited by the thermal expansion coefficient mismatch between AlSb and GaAs.   For AlSb growth a compressive strain develops which increases with increasing layer thickness.   Also, the growth rate for AlSb by MBE is only about 0.5 µm/hr.   It is for these reasons that the AlSb layer is restricted to 5 microns or less during this study.

Because AlSb oxidizes so rapidly, a protective layer of GaSb was applied as the last epitaxial step in the growth structure.

Before the diode structure was grown, a simplified sample (L11-37) was produced which consisted of AlSb sandwiched between the oxygen protective layer and the substrate.   A smoothing layer of GaAs was grown on the substrate to make the surface atomically flat

27

prior to AlSb growth. This structure, illustrated in figure 19, was used to perform electrical characterization measurements of the AlSb nucleation layer.
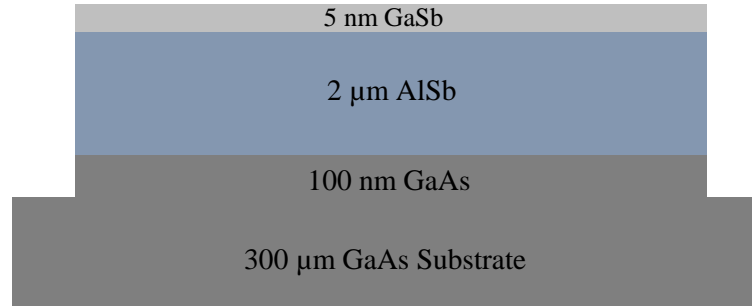
Figure 19.   L11-37 growth structure

To produce the diode structure, an n+ doped GaAs substrate was used and the final GaSb layer was p+ doped. Also, metallic ratios were applied during processing to provide ohmic contact layers, which allows for charge to flow easily in both directions on each electrode. The resulting thin film AlSb structure is illustrated in figure 20 below. Two samples were produced with this structure, called R12-23 and R12-50.
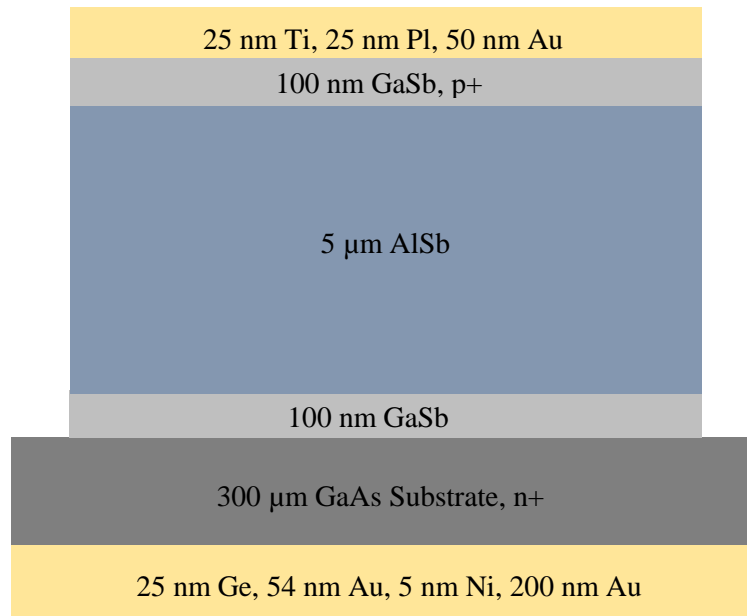
Figure 20.   Diagram of thin film AlSb diode structure, representative of samples R12-23 and R12-50

28

Chapter 5:   Characterization

While many methods are used to measure surface characteristics, crystal composition, defects, and electrical qualities, only the techniques used in this research will be summarized.   This chapter will discuss characterization results from AlSb grown in this study.   Table 4, below, outlines the samples used and associated production, described in the previous chapter, and characterization details presented in the following tables and figures.

Table 4.   Structure and characterization details for samples used

Sample Name	Structure Diagram	Characterization Methods Used / Results
L11-37	Fig. 19	Hall Effect / Table 5
R12-23	Fig. 20	Nomarski / Figure 21 XRD / Figure 28 I-V Curves / Figure 33
R12-50	Fig. 20	Nomarski / Figure 22 AFM / Figure 25 XRD / Figure 27 I-V Curves / Figure 34

5.1 Surface: Nomarski, AFM

All surface measurements were performed using diode structures R12-23 and R12-50 prior to the application of ohmic contact layers.

Nomarski imaging provides nondestructive topographical information on a microscopic scale by taking advantage of the interference contrast of two images of the same surface

area. Height differences are measured using the gradient of the refractive index and an image is produced that accentuates edges and boundaries on the surface [5]. Different levels of magnification can be used to examine surface characteristics over a wide range of dimensions. The following images in figures 21 and 22 depict features observed at different levels of magnification for R12-50 and R12-23, respectively.

10x

20x

50x
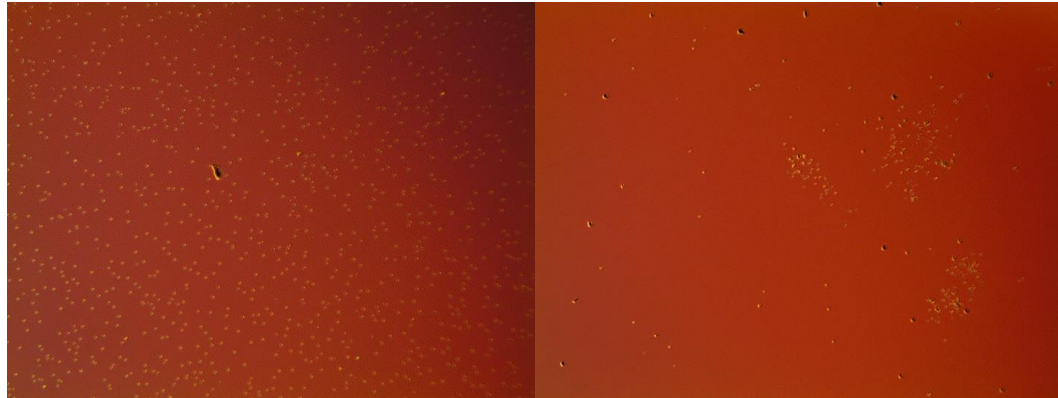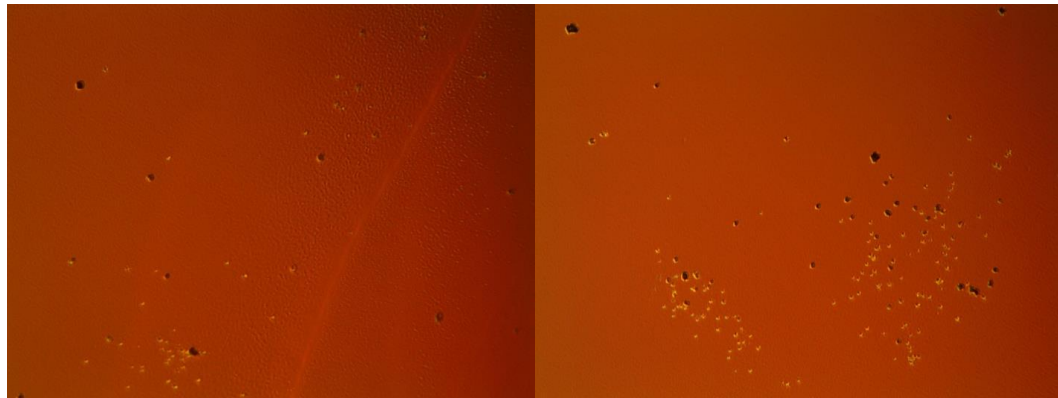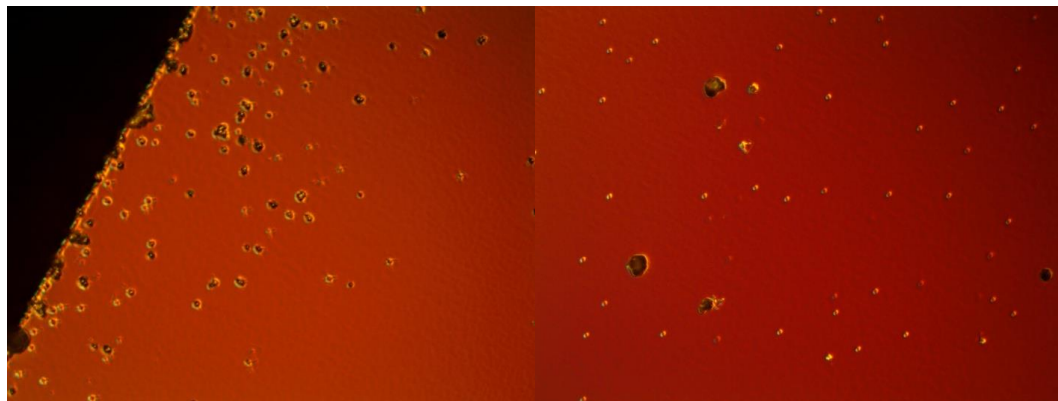
100x
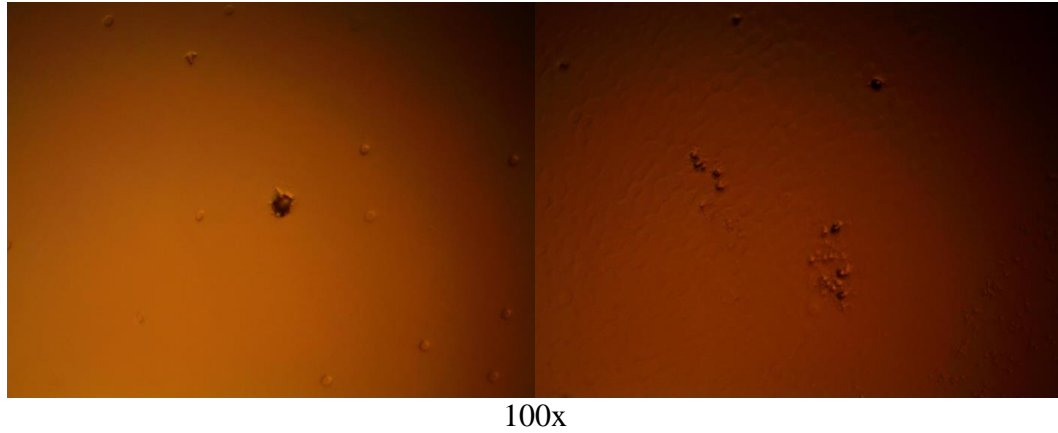
Figure 21.   Nomarski images of sample R12-50 at 10, 20, 50 and 100 times magnification

10x   50x
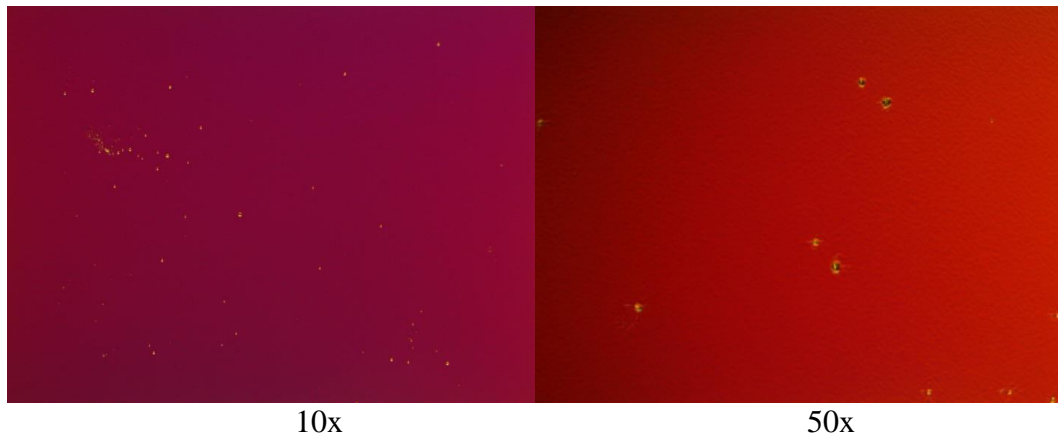
Figure 22.   Nomarski images of sample R12-23 at 10 and 50 times magnification

The circular pits on each optical image are crystal surface defects, more concentrated near the edge, which are expected when growth is non-homogeneous.   However, these pits may contribute to electrical shorting through the material when a bias is applied.   The "orange peel" texture, normal during antimony growth on arsenides, is representative of a roughened surface appearance due to wrinkle-like defects.   A comparison between the two samples for 10x and 50x magnification reveals a higher defect density on the surface for R12-50, which suggests that it is more likely to have electrical shunting issues.

Atomic force microscopy (AFM) also provides surface data.   The digital images are produced by measuring the small, but constant, force of a diamond tip as it scans across

31

the material surface being examined [5]. For increased understanding, a diagram of the AFM instrument is provided in figure 23.
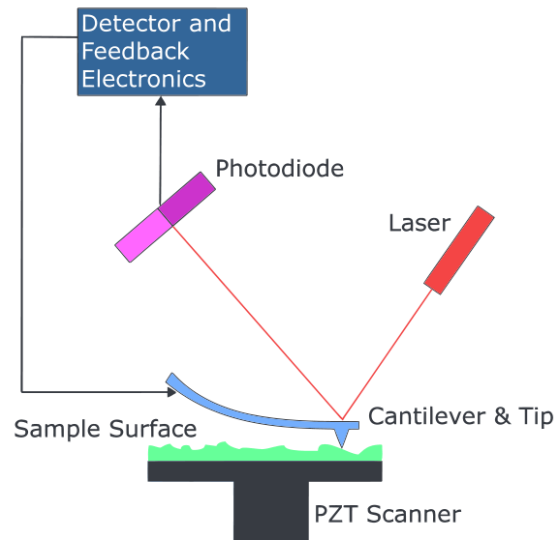
Figure 23.   Block diagram of AFM

Screw dislocations are a result of shear strain between lattice-mismatched layers. To relieve stress, the atomic layers begin to shift by one atom in a spiral staircase fashion, as is illustrated in figure 24 below [5]. The spiral features on the AFM images in figure 25 indicate the existence of screw dislocations, which is common (but not desirable) for heteroepitaxial growth structures, especially those involving antimonides and arsenides. The AFM images confirm that the AlSb growth is typical and there are no issues.
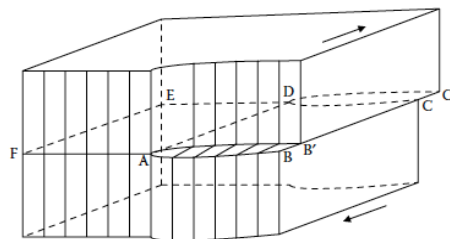
Figure 24.   Screw dislocation [5]

32
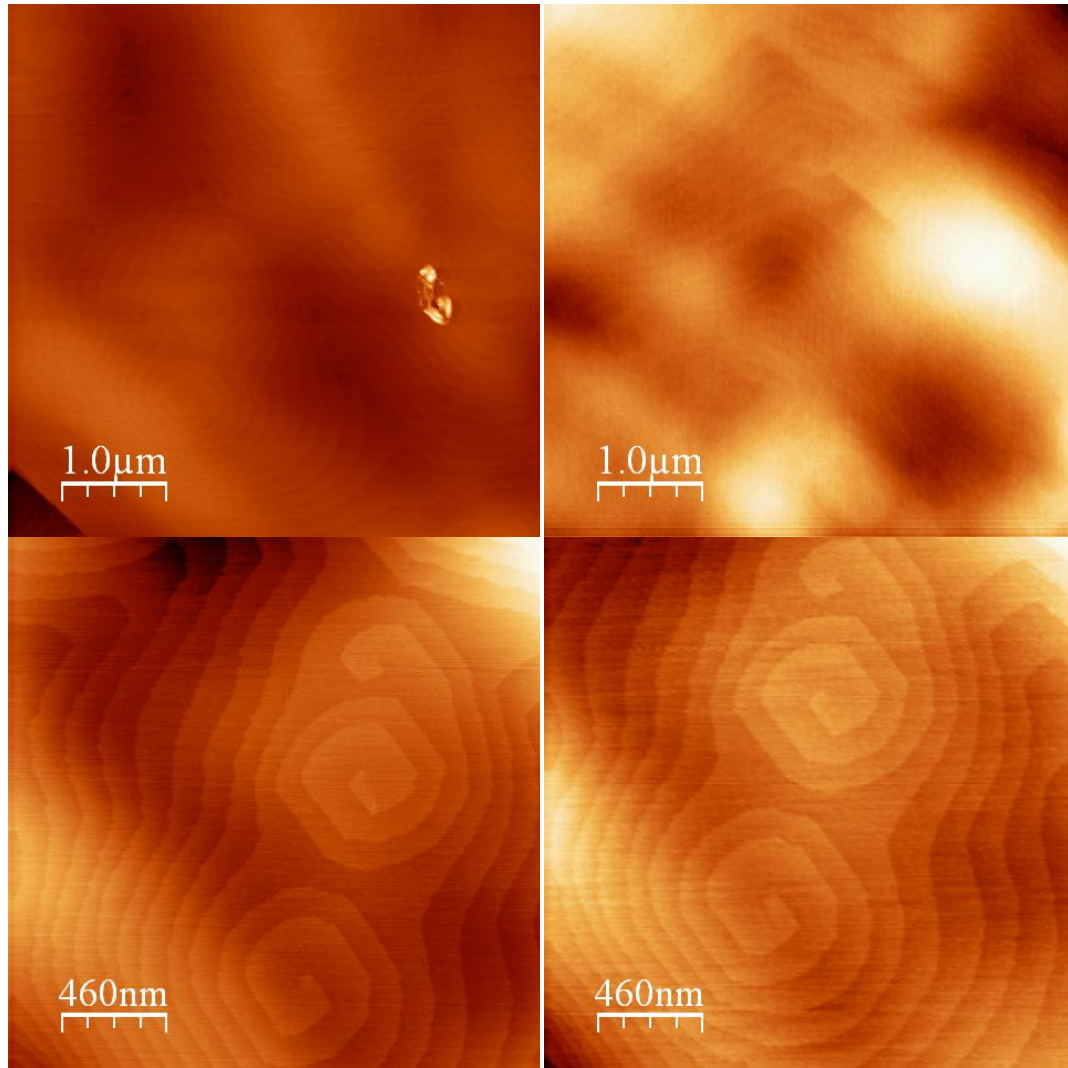
Figure 25.   Atomic Force Microscopy images for sample R12-50

5.2 Material Composition: X-Ray Diffraction (XRD)

Material composition measurements were also performed using the diode structures R12-23 and R12-50 prior to the final processing step of applying ohmic contacts.

Bragg scattering is used to evaluate the regularity of the crystal lattice.   With a perfect lattice, the scattering maxima follow the Bragg scattering equation, $n\lambda = 2d\sin\theta$.   An x-ray beam of wavelength λ is scattered off of the surface of a crystal at an angle θ and the reflected beam is measured.   The distance between atomic layers in the crystal (lattice

constant) is d, and n is an integer.   Bragg's law describes the difference in path length for scattering of x-rays with atoms of different crystal lattices, shown in the diagram in figure 26.
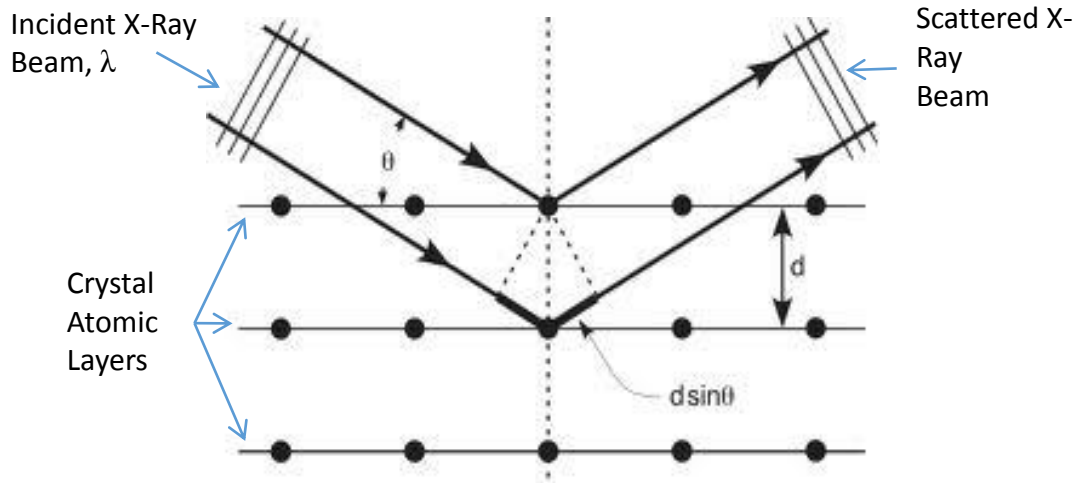
Figure 26.   Bragg Scattering, $n\lambda=2d\sin\theta$

For imperfect crystals, the distance between lattice points, the lattice constant, will vary, resulting in broadened reflection maxima.   The XRD characterization plot is presented in figure 27 for R12-50, where a sharp peak at 32.5° is observed on the right which represents the GaAs substrate with a lattice constant of 5.65 Å.   The farthest left peak near 29.5° is associated with the AlSb layer with a lattice constant of 6.13 Å, while the broadest peak around 30° represents the 100 nm GaSb capping, with a lattice constant of 6.09 Å. The layering is shown in Fig. 20.   The relative low intensity of the GaSb peak indicates that there is less material represented, which is expected since it is the thinnest layer of the structure.   The AlSb shows a sharp scattering peak indicative of good crystal structure. The relative sharpness of the AlSb peak compared to the GaSb peak suggests that the GaSb layers contain more strain related defects than the AlSb layer.   While the AlSb peak is not as narrow as that of the GaAs substrate, it does appear to have a fairly regular lattice, indicating good epitaxial growth with very little residual strain.

34
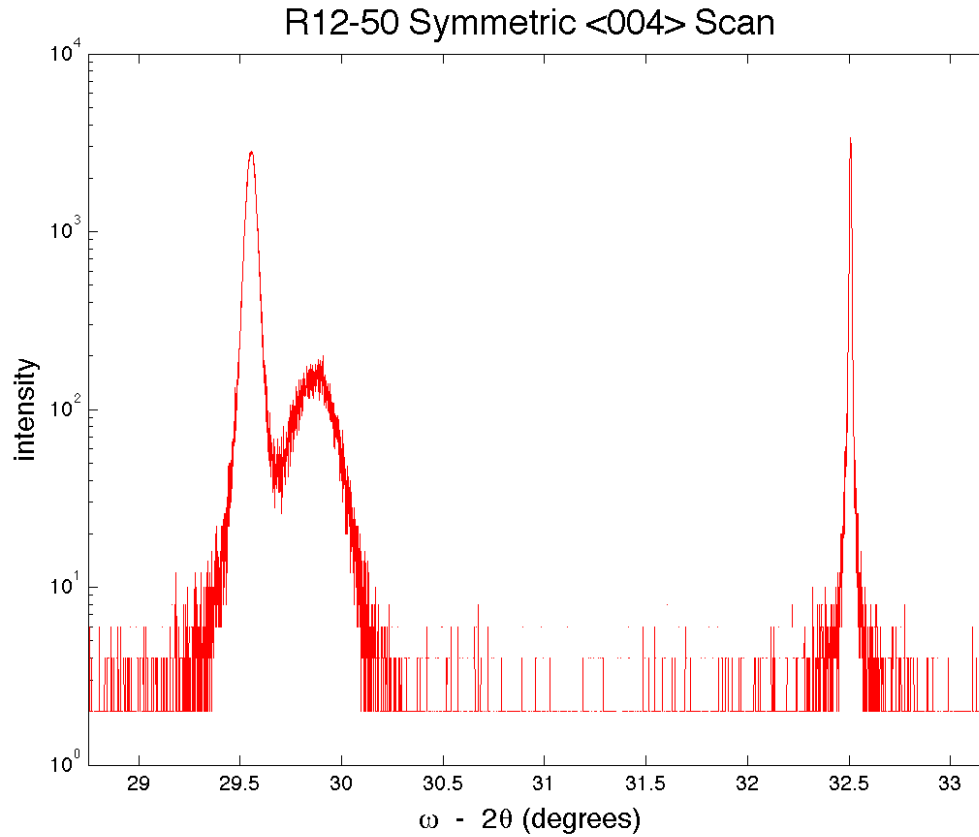
Figure 27.   XRD measurement of sample R12-50

The measurement for R12-23 is shown in figure 28, where the horizontal axis has been converted to arc seconds.   The layering is the same as for sample R12-50 (see Fig. 20). The AlSb and GaSb scattering peaks for sample R12-23 are wider than seen for the R12-50 sample.   XRD analysis of the two diode samples suggests that R12-23 has more residual strain in the AlSb layer and more tensile strain in the GaSb capping layer when compared to R12-50.
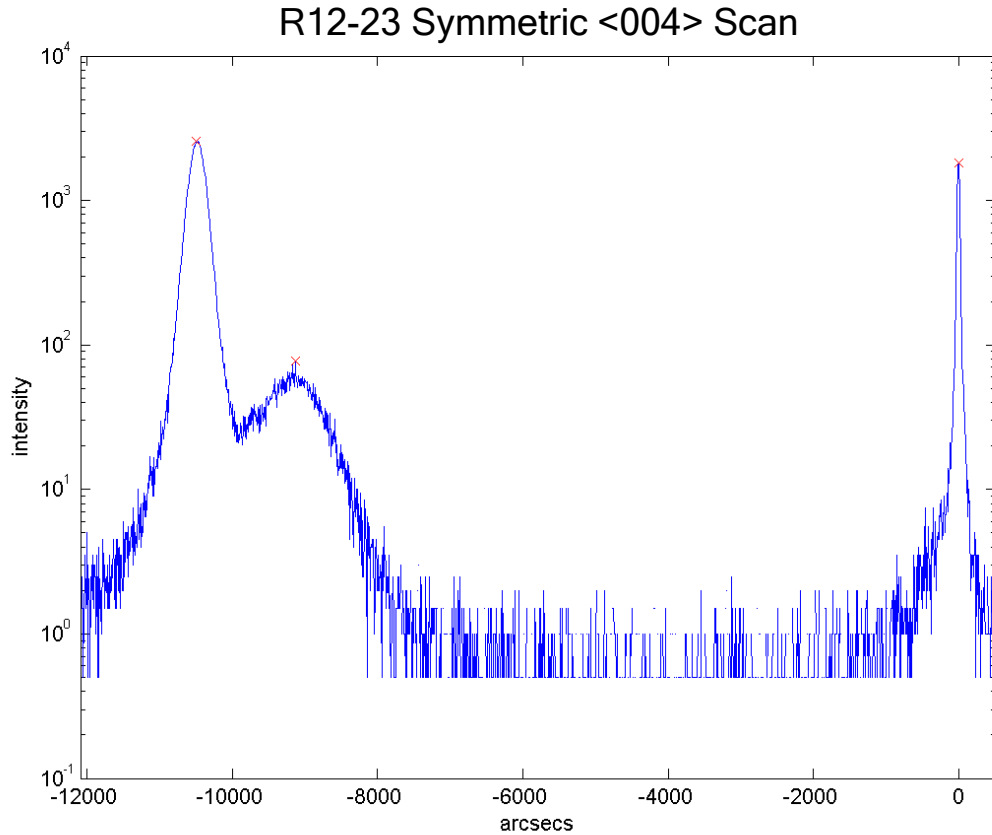
Figure 28.   XRD measurement of sample R12-23

5.3 Electrical Measurements: Hall Effect, I-V Curves

Hall-coefficient measurements are used to obtain the concentration and mobility of charge carriers [35].   This research employed the use of the van der Pauw technique for measuring the voltages.   Small ohmic contacts (indium) were annealed to each corner of the top (non-substrate) surface of a 1 cm^2 sample and it was placed in a magnetic field, B, normal to the surface.   As shown in figure 29, the resistances, R_A and R_B, between neighboring contacts can be calculated from the ratios of measured voltage, V, to applied test current, I.

36
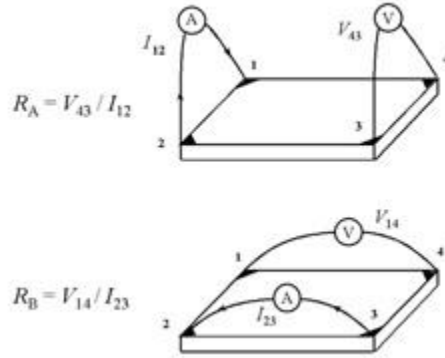
Figure 29. A schematic of a rectangular van der Pauw configuration [36]

The sheet resistance, R_S, is related to R_A and R_B through the van der Pauw equation, below, where $n = n_s/d$ is the bulk density of charge carriers (n_s is the sheet density and d is the conducting layer thickness). After numerically solving for R_S, the bulk electrical resistivity can be calculated using $\rho = R_S d$. [36]

$$e^{-n\left(\frac{R_A}{R_S}\right)} + e^{-n\left(\frac{R_B}{R_S}\right)} = 1 \tag{10}$$

Resistivity, ρ, is a material property that is highly temperature dependent, and in semiconductors is strongly affected by the presence of impurities. It can also be expressed as the inverse of the electrical conductivity, σ, of a given material, or $\rho = 1/\sigma$. A higher resistivity will reduce leakage current and allow for a depletion region under reverse bias, making it critical for a semiconductor detector.

To find the sheet carrier density, n_s, the Hall voltage, V_H, is measured across opposing contacts, as shown in figure 30. The sign of V_H is determined by the majority carrier type, where it is positive for holes and negative for electrons.

37
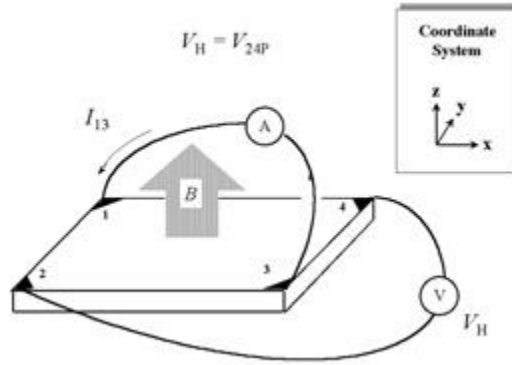
Figure 30.   Hall measurement schematic [36]

The mobility can be determined from the previously discussed Hall measurements using equation 11, where q $(1.602\times10^{-19}\,C)$ is the elementary charge.

$$\mu = \frac{|V_H|}{R_S I B} = \frac{1}{q n_s R_S} \tag{11}$$

A test current, I, was applied through one set of opposing contacts while V_H is measured across the remaining pair of contacts.   Then the process was repeated with opposite applied test current and measured voltage diagonals, so there are two measurements for each test current run.   Similar results for the two measurements indicate good sample test preparation.

The Hall effect measurement results are outlined in table 5, which is an analysis of sample L11-37 taken at room temperature.   The majority carrier was revealed to be holes (V_H was positive), revealing the extreme p-type nature of the AlSb grown in this study.   Because the average carrier concentration values are so high, it is suspected that Sb interstitials exist in the lattice, resulting in much higher hole concentrations than anticipated and the AlSb layer in the intended P-I-N diode not behaving like an insulator.   This may contribute to tunneling effects, or Zener breakdown, when even a low reverse bias is applied.

38

Table 5. Hall effect measurements for sample L11-37, taken at room temperature

Test Current [µA]	Average Carrier Concentration [cm³]	Average Carrier Mobility [cm²/Vs]	Resistivity [Ω-cm]
100	5.65E+18	141.9	8.452E-03
	5.81E+18	134.86	8.636E-03
200	1.83E+19	64.59	7.975E-03
	5.04E+19	15.56	6.622E-03
500	9.42E+18	82.72	8.106E-03
	1.31E+19	75.03	6.716E-03
500	7.37E+18	107.37	7.940E-03
	5.75E+18	139.84	6.296E-03
750	1.07E+19	78.23	8.003E-03
	1.06E+19	84.51	7.131E-03

Lower than expected values for mobility and resistivity were also observed. As was presented in table 2, the hole mobility is theorized to be as high as 700 cm^2/Vs, while measurements revealed about 100 cm^2/Vs. For germanium, silicon and CZT detectors, materials have been produced with resistivity as high as 47 Ω-cm [29], 10^6 Ω-cm [29], and 10^{10} Ω-cm [38, 39] at room temperature, respectively. A lower resistivity leads to a higher leakage current and a higher operating noise level, making smaller signals harder to discern. We were pushing for a resistivity of at least 10^5 Ω-cm, to compete with thin film silicon surface barrier detectors [40, 41] at room temperature, which we are far from with the current growth, having an average measured resistivity of 8×10^{-3} Ω-cm.

Both mobility and resistivity properties change as a function of majority carrier concentration, as is evidenced by the plots in figures 31 and 32 [45]. Our carrier concentration was 10^{19} per cm on average, corresponding to a mobility of a little more than 100 cm^2/Vs according to the bottom curve in the top plot in figure 31, which is representative of p-type germanium. The mobilities for silicon (center) and GaAs (bottom) are even lower at this concentration. Similarly in figure 32, 10^{19} holes/cm^3 corresponds to a resistivity of about 2×10^{-3} Ω-cm for p-type germanium and 8×10^{-3} Ω for

39

p-type GaAs.   So the Hall measurements appear to be representative of extremely p-type AlSb.
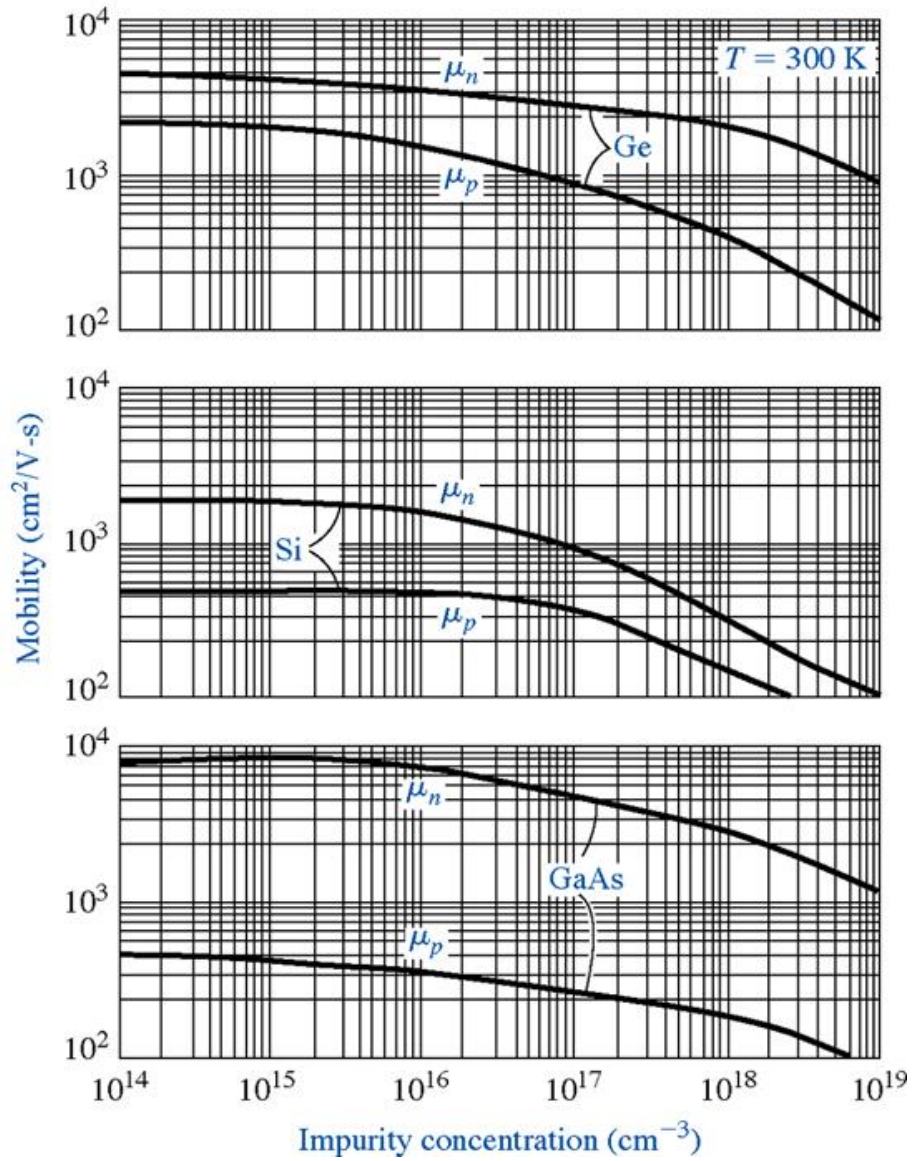
Figure 31.   Mobility as a function of impurity concentration for germanium (top), silicon (center) and gallium arsenide (bottom) [45]

40
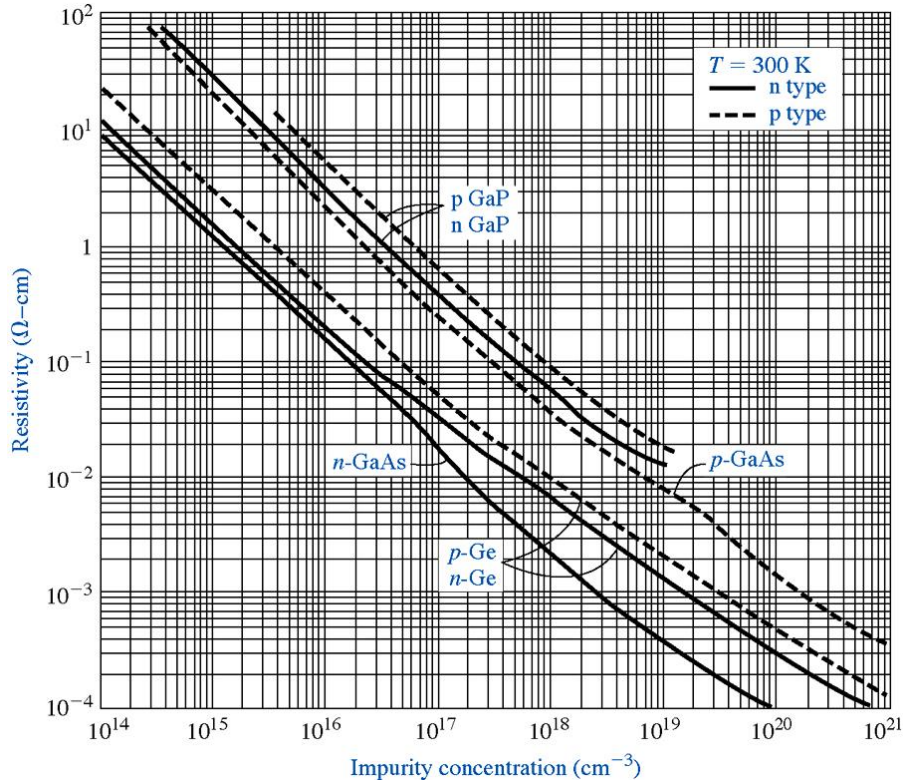
Figure 32. Resistivity as a function of impurity concentration for several semiconductor materials [45]

I-V curves provide information about the performance expectation, the leakage current in particular, for semiconductor devices. In an effort to reduce the concentration of electrical losses due to dislocations produced during growth, the sample was cleaved into smaller pieces. These are labeled a through d in the plot in figure 33. Measurements were performed for R12-50 (annealed and non-annealed) cleaved pieces as well, also shown below in figure 34. Overall, the I-V curves for R12-23 look less leaky than the curves for R12-50. This may be associated with a larger defect density (observed in the Nomarski images) for R12-50, which is known to contribute to electrical shunting issues.

41
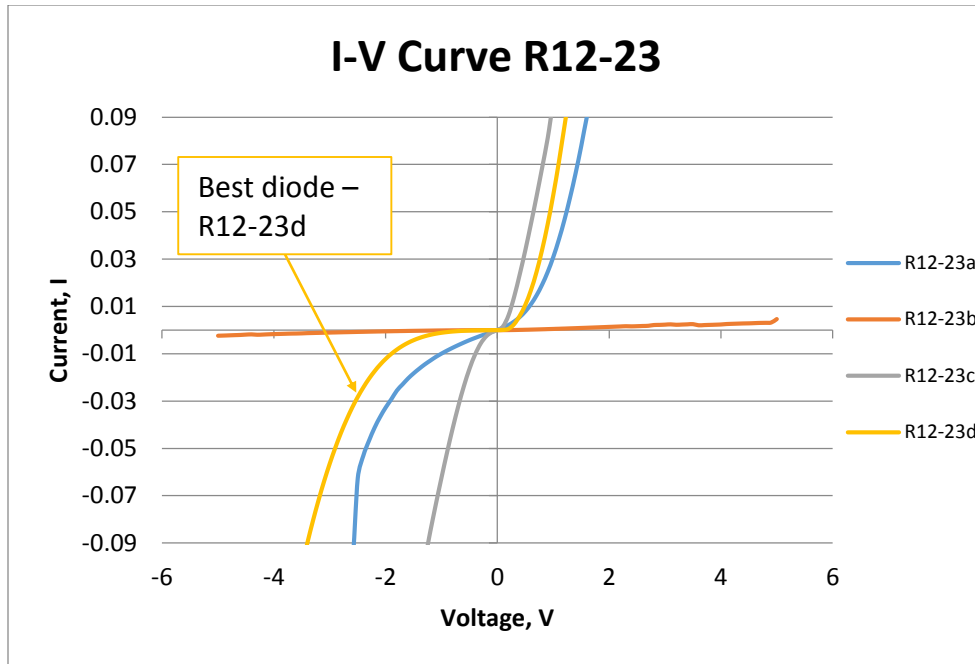
Figure 33.   Measured I-V curves for cleaved pieces of sample R12-23
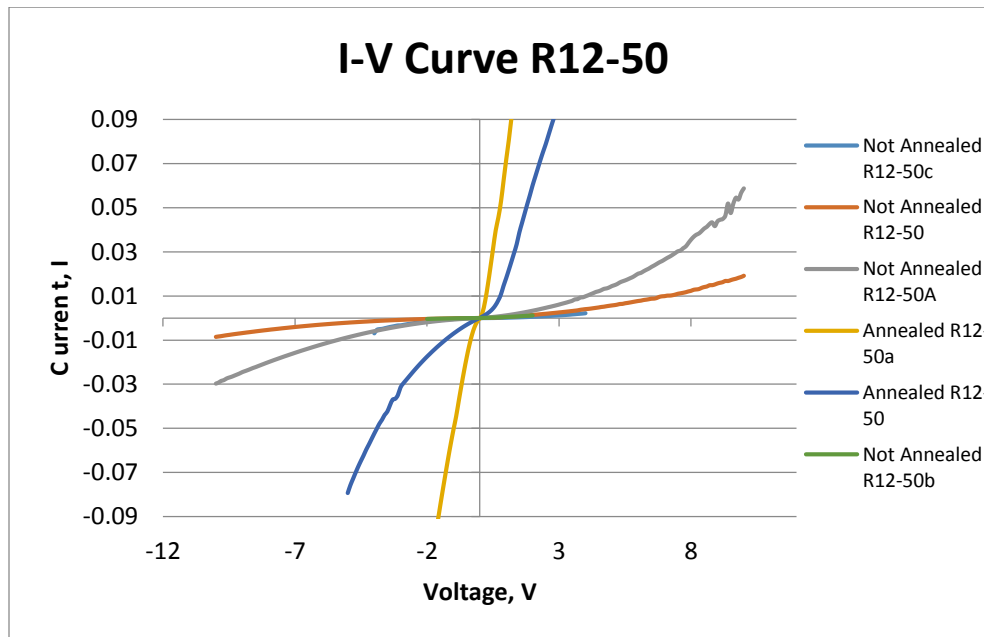
Figure 34.   Measured I-V curves for cleaved pieces of sample R12-50.   The sample was divided, and then one half was annealed, before cleaving into smaller pieces.

Although all samples were used, R12-23d had an I-V curve most resembling that of a diode with decreased leakage compared to the other samples. Figure 35 illustrates a typical I-V curve shape for a diode (left), where the Zener breakdown and avalanche breakdown curves are indicated in the reverse bias region, compared to the curve for R12-23d (right).
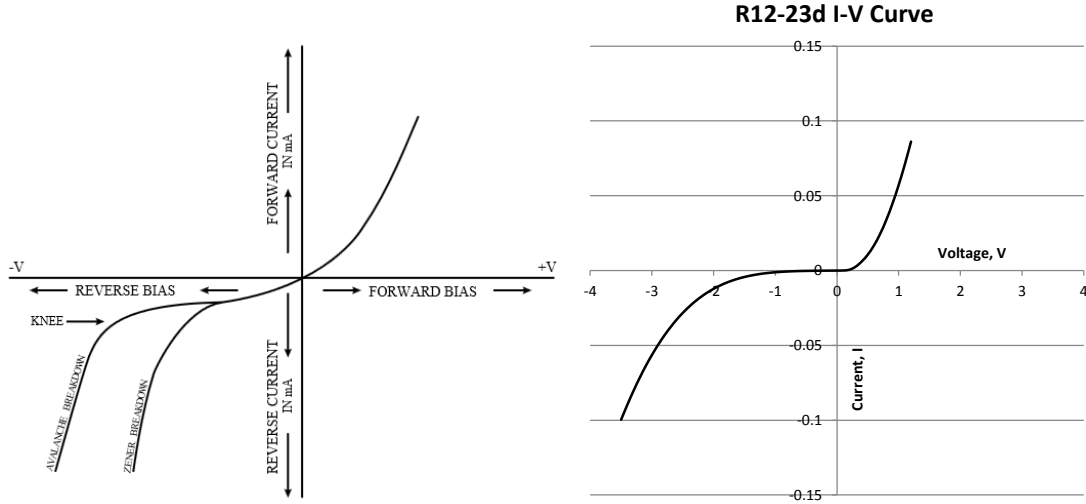
Figure 35.   Typical IV curve for a diode (left) compared to R12-23d (right)

The maximum voltage sustainable without current breakdown is the full depletion voltage, V_{FD}, which is the minimal operation value for depletion through the volume of the active region.   The equations for voltage and electric field, E(x), at full depletion are given below in equations 12 and 13, respectively, for planar diode geometry, where D is the depletion depth, T is the detector thickness, ρ is the charge distribution (ρ=-eN_A), and ε is the dielectric constant.   The maximum electric field, E_{max}, occurs when T=D and x=0. Applying this condition and inserting equation 12 into equation 13 for V, we get equation 14 for E_{max}. [8]

$$V_{FD} = \frac{\rho T^2}{2\varepsilon} \tag{12}$$

$$E(x) = \frac{V}{2D} + \frac{\rho}{\varepsilon}\left(\frac{D}{\varepsilon} - x\right) \tag{13}$$

43

$$E_{max} = \frac{2V_{FD}}{D} \tag{14}$$

According to the measured curve for R12-23d, a reverse bias of less than about 1.5 V should be used to reduce the leakage and prevent potential damage to the material. This is a low voltage, but for a depletion depth of about 5 microns, this is an electric field of about 6000 V/cm, using equation 14. For comparison, HPGe detectors are operated near 2000 V/cm for a reverse bias voltage of 1000 V and a 1 cm depletion depth. Thin film (~300 μm) silicon detectors with an effective full depletion voltage of 40 V have an E_{max}=3000 V/cm.

Extrapolating the forward bias curve down to 0 current in figure 35 gives a "turn on" voltage of about 0.5 V. Following the rough formula of $V_{turn\ on} = E_{gap} - 0.7$ eV, this is indicative of diode behavior more likely occurring between the GaSb and GaAs, where $V_{turn\ on}$ is expected to be about 0.4 V (for an average E_{gap} of about 1.1 eV). For depletion through the AlSb we expect a $V_{turn\ on}$ closer to 0.9 V. Therefore, the depletion region may be restricted to the GaSb.
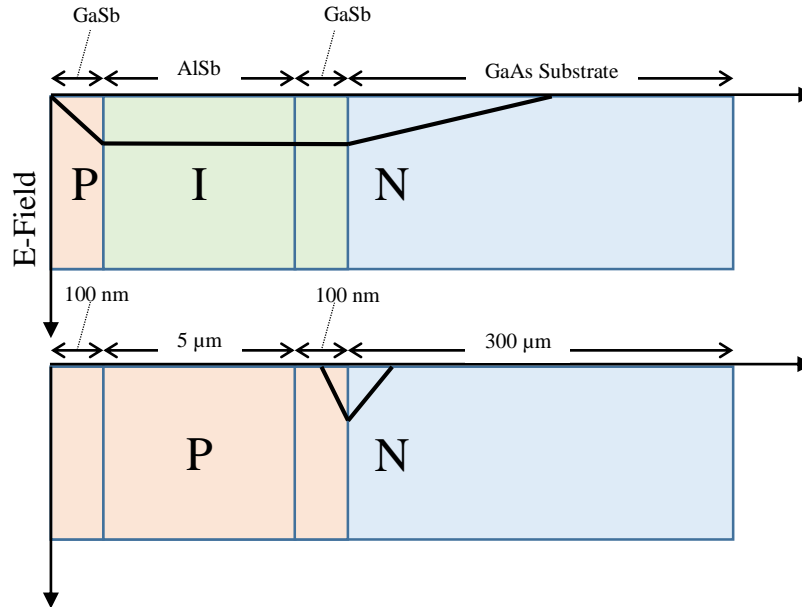
Figure 36.   Intended PIN electric field (top) and suspected electric field (bottom) in sample R12-23d as deduced from extrapolation of the "turn-on" voltage from the I-V curve

44

The high leakage current on the reverse bias side of the curve in figure 35 may be due to Zener breakdown, where the depletion region may be too narrow and the electrons/holes tunnel easily across the junction. Diagrams of the induced electric field under reverse bias for the intended PIN junction (top) and suspected PN junction (bottom) structures are shown in figure 36.

The expectation was that the AlSb would behave like an insulator between the GaSb p+ doped cap region and the GaAs n+ doped substrate region, with a GaSb strain relief layer between the AlSb and GaAs substrate. Due to the inherent p+ nature of the grown AlSb layer, the depletion region may be set up between the unintentionally p+ type AlSb and intentionally n+ type GaAs, partially depleting the GaSb strain relief layer. This suspicion is reinforced by a calculation of the depletion width for a P-N junction with doping densities on the order of 10^{19} cm^{-3} at room temperature, following equations 15 and 16 for intentional doping.

$$W = x_p + x_n = \sqrt{\frac{2\varepsilon}{q} V_0 \left(\frac{1}{N_A} + \frac{1}{N_D} \right)} \tag{15}$$

$$V_0 = \frac{kT}{q} ln \left(\frac{N_A N_D}{n_i^2} \right) \tag{16}$$

For GaAs without any bias, V_0=1.0781 V and W=0.0203 µm (~20 nm). With an applied voltage of -2 V the depletion width is increased to 0.031 µm (~30 nm), which is still very much restricted within the GaSb layer, as the P-N structure in figure 36 illustrates. In contrast, for reasonable carrier densities on the order of 10^{15} cm^{-3}, the depletion width is 1.6824 µm and 2.8833 µm with and without a -2 V bias, respectively, which would deplete (at least partially) through the AlSb layer.

This can be corrected so the depletion region extends between the cap layer and the substrate, across most of the AlSb, by a higher purity AlSb or intentionally n+ doping the AlSb to compensate.

Chapter 7:   Radiation Detection Evaluation

7.1 Experimental Procedure

To experimentally evaluate the response to radiation, the structure was exposed to sealed sources while a reverse bias was applied.   The sources used include Ba-133 and Co-57 for gamma/x-rays, and Am-241 for alphas.   Measurements were conducted using a variety of pre-amps, several means of supplying power, and an oscilloscope.   A schematic of the experimental setup is illustrated in figure 37.
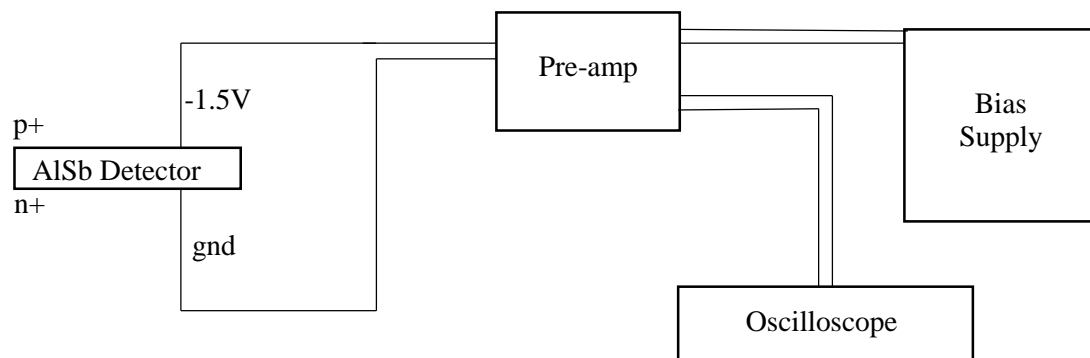
Figure 37.   Experimental Diagram

The diode structure was placed on a copper plate with the substrate face touching the surface, allowing the thinner ohmic contact layer to be exposed to the incident radiation. A negative bias voltage was applied to the p+ side of the diode via the probe tip attached to the center wire of coaxial cable, while the n+ side was grounded to the sheath wire. The coaxial cable was then fed from the pre-amp to an oscilloscope where a pulse should be observed.   The radionuclide sources were adjustably placed above the p+ surface of the diode, as seen in figure 38.

www.manaraa.com
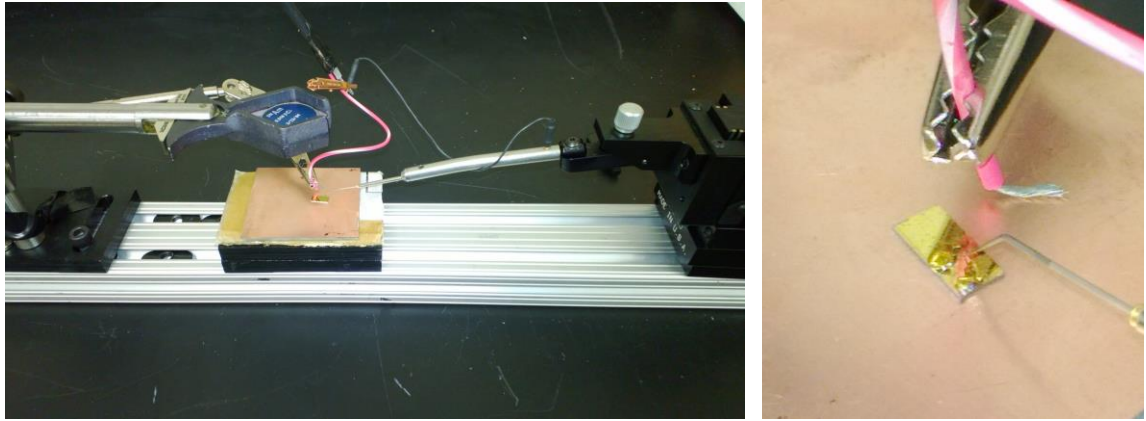
Figure 38.   AlSb detector setup, shown with R12-23d

To reduce noise interference from ambient signals in the lab, the probe setup was placed inside a sealable metal chamber (i.e., an air filled vacuum chamber) as a Faraday cage, and the coaxial cable was fed through electrically isolated connectors.   Exposed connection sites were wrapped in aluminum foil. To minimize electronic noise, an examination of available pre-amps was performed using the SSB detector exposed to alphas from Am-241. Alpha particles are highly interacting and expected to deposit several MeV of energy in the thin AlSb layer.   The results are summarized in table 6.

Table 6.   Peak to peak noise observed on oscilloscope from available pre-amps in lab, using SSB 27-473G (BA-15-25-1500) and Am-241 source

Pre-amp Name/ Model #	Noise w/o source or voltage applied	Noise with 50 V, no source	Baseline "jumps" with voltage adjustment	Signal/Noise with Am-241 source, w/o voltage	Signal/Noise with Am-241 source, with 50 V
109A Ortec (1x)	5 mV	2 mV	Yes	30mV / 5mV	37mV / 2mV
109PC Ortec (1x)	50 – 75 mV	1.5 mV	Yes	30mV / 3mV	30mV / 1.5mV
142 Ortec	15 mV ringing, 5 mV baseline	15 mV ringing, 3 mV baseline	Yes	60mV / 5mV	60mV / 3mV
142PC Ortec	50 mV	30 mV	Yes, but small in comparison to others	450mV / 50mV	600mV / 30mV
142PC Ortec (newer)	30 mV	25 mV	Yes	500mV / 30mV	650 mV / 25mV

47

An additional pre-amp, RIS, was also used to measure the signal through a SSB from Am-241. Ringing was observed with the RIS pre-amp and the signal to noise ratio was 65 mV/5mV using SSB 9-722 and 18 V supplied by two 9 V batteries. A baseline "jump" was also observed when the voltage was adjusted. Based on the evaluation, the two 142 Ortec preamplifiers had the best signal to noise ratios.

Using the 142 Ortec preamp (listed third in table 6) and R12-23d, without connecting the bias wire to the structure, the baseline noise was about 3 mV peak to peak. When the reverse bias was connected the baseline became jumpy and the noise increased to 5-7 mV peak to peak. This is the opposite effect experienced with the SSB (where the noise was reduced after introducing the reverse bias). The outcome was not changed by the application of a forward bias (rather than a negative bias). Next, the Am-241 source was introduced, but no changes were observed. The other sources, pre-amps, and AlSb pieces were also tested without noticeable differences between the presence and absence of a radionuclide source.

7.2 Current Signal Shape

To predict the signal current pulse shape, which we're trying to read out above the noise, the total depletion depth transit time and signal amplitude was calculated using the following procedure. The diagram in figure 39 illustrates the motion of electrons and holes in the depleted region of a semiconductor under reverse bias. The following derivation is summarized from Bertolini's chapter, Pulse Shape and Time Resolution, in Semiconductor Detectors [29].

48
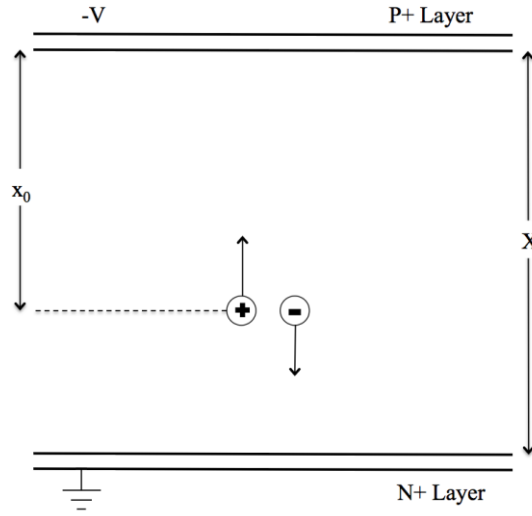
Figure 39.   Motion of charges in the depleted region of a semiconductor [29]

First, the electric field in the depletion region is said to be constant and equal to the applied bias, V, divided by the compensated thickness, X.

$$E_{Field} = -\frac{V}{X} = constant \tag{17}$$

The induced charge, Q, derived from Ramo's theorem, is then calculated for electrons and holes, where x_0 is the distance from the cathode where the electron-hole pair is generated.

$$Q_n(t) = e\frac{(X - x_0)}{X}t \quad for\ electrons \tag{18}$$

$$Q_p(t) = e\frac{x_0}{X}t \quad for\ holes \tag{19}$$

Solving for the collection times, t, and using the mobilities for electrons and holes we get the next equations. [29]

49

$$t_n = \frac{(X - x_0)}{\mu_n E_{Field}} \quad and \quad t_p = \frac{x_0}{\mu_p E_{Field}} \tag{20}$$

For the longest hole transit distance $x_0 = X = 5$ microns (or electron distance $x_0 = 0$), and assuming a symmetric mobility of 100 cm^2/Vs, the maximum transit time, t_c, is 1.67 ns. This is also known as the output signal rise time.

The Shockley-Ramo theorem states that the instantaneous current induced on a given electrode equals the product of the charge of the particle, its velocity and the component of the electric field in the direction of the velocity vector.

$$i = q * (v) \bullet (\bar{E}_0) \tag{21}$$

Using the maximum electric field calculated in the previous chapter ($E_{max} = 6000$ V/cm), the carrier velocity $v = \mu/X = 2 \times 10^5$ cm/Vs (for a depletion region 5 microns wide and $\mu = 100$ cm^2/Vs), and estimating absorbed and excitation energies of 5 keV and 5 eV, respectively,

$$q = ne = \left(\frac{absorbed\ energy}{excitation\ energy}\right)e = 1000\ electrons \tag{22}$$

$$i = (1000\ e^-)(2 \times 10^5\ cm/Vs)(6000\ V/cm) = 1.2 \times 10^{12}\ e^-/s$$
$$\tag{23}$$
$$1\ Amp = 6.25 \times 10^{18}\ e^-/s$$

$$i = 1.92 \times 10^{-7} A \approx 0.2\ \mu A.$$

To predict the measurable current pulse height, the impedance of the cable going into the oscilloscope is needed. Assuming a minimum resistance (for maximum pulse height) of 50 Ω, V = IR = 9.6×10^{-6} V ≈ 10 μV = 0.01 mV. This predicted signal is less than 1% of the minimum noise measured and so it is unlikely that we can detect signals with the current samples. For alpha particles, simulations show about 1 MeV of energy deposited in the

50

AlSb. This translates to a signal of approximately the size of the noise for the quietest preamplifier, making it difficult to discern from noise. A depletion region in the AlSb and reduced noise from leakage current is needed.

Chapter 7: Results

Surface characterization measurements indicated that there were screw dislocations and an orange peel like texture. XRD analysis suggests that the AlSb layer has good lattice structure. The Hall measurements revealed values lower than expected for both resistivity and charge carrier mobility, likely due to unintentional p+ doping of the AlSb during growth, making it unlikely to detect a signal above the leakage current fluctuations. I-V curve results had Zener breakdown characteristics, showing a large leakage current for most of the processed samples. Predicted signal current pulses, based on energy deposition and collection timing, were obscured by observed background levels due to leakage current. Thus, we have not been able to observe clear indications of pulses due to radiation.

These experiments have shown the difficulty of pure and defect free AlSb growth. We have not yet reached the theoretical promise. Many critical material properties measured by other researchers have also been significantly poorer than theorized expectations. It is worth mentioning that the success experienced with HPGe and CZT detectors is a direct result of many years of laboratory research to improve the growth and purification of these materials. Consequently, AlSb should not be ruled out as a material candidate for use as a radiation detector. The following chapter will address future studies that should be performed to further evaluate AlSb.

Chapter 8:   Future Work

To fully determine whether AlSb is a suitable material for radiation detectors, every parameter must be examined and optimized.   Ultimately, more pure and defect free growth is required to increase resistivity, thus allowing for a depletion region in the semiconductor and drastically reducing leakage current.   Successful spectroscopy is based on good signal to noise ratios, and the predicted signal is understood to be on the order of below noise levels of the leakage current in the samples examined.

8.1 Compensation Doping or Higher Purity AlSb

The AlSb produced to date has had unintentional p+ doping.   As explained in chapter 6, this reduces the depletion region to a small sliver in the GaSb strain reduction layer.   To make the depletion region occur between the GaSb capping layer and the GaAs substrate, the AlSb may be made more pure or may be compensated with n+ doping to correct for the unintentional p+ doping.   Another method of influencing the hole concentration is adjusting the substrate temperature during MBE growth.

Reducing the hole concentration or improvements in material purity could be useful for increasing resistivity properties.   An iterative study on the effect of compensation doping or growth temperature changes using Hall measurements should be conducted to optimize the charge transport properties of the AlSb layer.   Such procedures were not performed due to limitations on the scope, budget and time constraints of this project.

Appendix: MCNPX Input Files

Simulated Spectra Distributions

```
Ba-122 Decay Energy Distribution:
SI1 L  0.00429 0.030625 0.030973 0.08  0.302851 0.356
SP1 D  0.163   0.351    0.643     0.341 0.1833   0.6205


Co-57 Decay Energy Distribution:
SI1 L  0.006409 0.006391 0.0144129 0.12206065 0.13647356
SP1 D  0.329    0.166    0.0916    0.856       0.1068
```

Co-57 source incident on 5 microns AlSb

```
AlSb semiconductor detector
c cell cards
20 200   -0.0013    -7  8   1        $  "            "
21 200   -0.0013    -7 -8   9        $Variance Reduction
22 200   -0.0013    -7 -9   10       $  "            "
23 200   -0.0013    -7 -10 11        $  "            "
24 200   -0.0013    -7 -11           $  "            "
30 500   -19.3      -1 -2            $Gold
40 400   -5.61      -1 -3 2          $GaSb
50 100   -4.26      -1 -4 3          $AlSb
60 400   -5.61      -1 -5 4          $GaSb
70 300   -5.32      -1 -6 5          $GaAs
80 500   -19.3      -1 6             $Gold
90 200   -0.0013     1 -7            $Air
100 0               7                $void

c surface cards
1  rpp        -1 1    -1 1          0 0.305584
2  pz 0.000100
3  pz 0.000200
```

54

```
4  pz   0.005200
5  pz   0.005300
6  pz   0.305300
7  rpp      -1.1 1.1   -1.1 1.1      -0.15 0.31
8  pz   -0.03
9  pz   -0.06
10 pz   -0.09
11 pz   -0.12

c data cards
nps 10000000
imp:p  1 1.23m 0.98m 1m 1 1 1 1 1 1 1 1 0
imp:e  1      1       1  1 1 1 1 1 1 1 1 1 0
mode p e
phys:p 100 1 0 0 0 0
m100    13027.04p        -0.5      $AlSb
        51000.04p        -0.5
m200     7000.04p -0.755636      $Air
         8000.04p -0.231475
        18000.04p -0.012889
m300    31000.04p        -0.5      $GaAs
        33074.04p        -0.5
m400    31000.04p        -0.5      $GaSb
        51000.04p        -0.5
m500    79197.04p        -1.0      $Gold
c - - - Materials - - - - - - - - - - - - - - - - - - - - -
m100    14000.04p        -1.0       $Si
m200    79000.04p        -1.0       $Au
m300     7000.04p -0.755636       $Air
         8000.04p -0.231475
        18000.04p -0.012889
c - - - Source - - - - - -Co-57 - - - - - - - - - - - - -
sdef pos=0 0 -0.14  par=2 erg=d1
SI1 L  0.006409 0.006391 0.0144129 0.12206065 0.13647356
SP1 D  0.329    0.166    0.0916    0.856       0.1068
c - - - Tallies - - - - - - - - - - - - - - - - - - - - -
f8:p 30
fmesh4*:p    geom=xyz    origin=-0.6 -0.6 -0.15
             imesh=0.6    iints=100
             jmesh=0.6    jints=100
             kmesh=0.006  kints=50
```

55

```
                    factor=5e18
FT8 GEB 0 0.02 0
e8 0 1e-5 1000ilog 0.4
```

Co-57 source incident on 50 microns Si SSB

```
Si detector with gold barrier layer
c cell cards
15 300 -0.0013      -3 -4            $ Var reduction cell
16 300 -0.0013      -3 -5 4          $   "                          "
17 300 -0.0013      -3 -6 5          $   "                          "
18 300 -0.0013      -3 -7 6          $   "                          "
19 300 -0.0013      -3  1 7          $   "                          "
20 200 -19.3        -1 -2            $ Gold
30 100 -2.33        -1  2            $ Si
40 0                 3              $ Void

c Surface cards
1 rcc  0 0 0    0 0 0.0051      0.5
2 pz    0.0001
3 rpp  -0.6 0.6   -0.6 0.6    -0.15 0.006
4 pz    -0.12
5 pz    -0.09
6 pz    -0.06
7 pz    -0.03

c data cards
nps 10000000
imp:p 1 2.06m 1.05m 1.05m 0.595m 2.04m 1.15m 0
imp:e 1    1    1    1    1     1     1 0
mode p e
phys:p  100 1 0 0 0 0
c - - - Materials - - - - - - - - - - - - - - - - - - - - -
m100    14000.04p      -1.0           $Si
m200    79000.04p      -1.0           $Au
m300     7000.04p -0.755636           $Air
         8000.04p -0.231475
        18000.04p -0.012889
```

```
c - - - Source - - - - - - -Co-57 - - - - - - - - - - - - -
sdef pos=0 0 -0.14  par=2 erg=d1
SI1 L  0.006409 0.006391 0.0144129 0.12206065 0.13647356
SP1 D  0.329    0.166    0.0916    0.856       0.1068
c - - - Tallies - - - - - - - - - - - - - - - - - - - - - -
f8:p 30
fmesh4*:p   geom=xyz    origin=-0.6 -0.6 -0.15
            imesh=0.6    iints=100
            jmesh=0.6    jints=100
            kmesh=0.006  kints=50
            factor=5e18
FT8 GEB 0 0.02 0
e8 0 1e-5 1000ilog 0.4
```

Ba-133 source incident on 5 microns AlSb

```
AlSb semiconductor detector
c cell cards
20 200   -0.0013    -7  8  1           $  "            "
21 200   -0.0013    -7 -8  9           $Variance Reduction
22 200   -0.0013    -7 -9  10          $  "            "
23 200   -0.0013    -7 -10 11          $  "            "
24 200   -0.0013    -7 -11             $  "            "
30 500   -19.3      -1 -2              $Gold
40 400   -5.61      -1 -3 2            $GaSb
50 100   -4.26      -1 -4 3            $AlSb
60 400   -5.61      -1 -5 4            $GaSb
70 300   -5.32      -1 -6 5            $GaAs
80 500   -19.3      -1 6               $Gold
90 200   -0.0013     1 -7              $Air
100 0                7                 $void

c surface cards
1   rpp     -1.0 1.0   -1.0  1.0     0.0  0.305584
2   pz  0.000100
3   pz  0.000200
4   pz  0.005200
5   pz  0.005300
```

57

```
6   pz   0.305300
7   rpp       -1.1 1.1    -1.1    1.1    -0.15 0.31
8   pz   -0.03
9   pz   -0.06
10  pz   -0.09
11  pz   -0.12

c data cards
nps 10000000
imp:p  1 1.23m 0.98m 1m 1 1 1 1 1 1 1 1 0
imp:e  1      1       1  1 1 1 1 1 1 1 1 1 0
mode p e
phys:p 100 1 0 0 0 0
m100    13027.04p        -0.5      $AlSb
              51000.04p        -0.5
m200     7000.04p -0.755636     $Air
               8000.04p -0.231475
             18000.04p -0.012889
m300    31000.04p        -0.5      $GaAs
              33074.04p        -0.5
m400    31000.04p        -0.5      $GaSb
              51000.04p        -0.5
m500    79197.04p        -1.0      $Gold
c - - - Materials - - - - - - - - - - - - - - - - - - - - - - -
m100    14000.04p        -1.0               $Si
m200    79000.04p        -1.0               $Au
m300     7000.04p -0.755636               $Air
          8000.04p -0.231475
         18000.04p -0.012889
c - - - Source - - - - - - - -Ba-133- - - - - - - - - - -
sdef pos=0 0 -0.14  par=2 erg=d1
SI1 L  0.00429 0.030625 0.030973 0.08  0.302851 0.356
SP1 D  0.163    0.351     0.643     0.341 0.1833    0.6205
c - - - Tallies - - - - - - - - - - - - - - - - - - - - - - -
f8:p 30
fmesh4*:p    geom=xyz     origin=-0.6 -0.6 -0.15
          imesh=0.6     iints=100
          jmesh=0.6     jints=100
          kmesh=0.006   kints=50
          factor=5e18
FT8 GEB 0 0.02 0
```

58

```
e8 0 1e-5 1000ilog 0.4
```

Ba-133 source incident on 50 microns Si SSB

```
Si detector with gold barrier layer
c cell cards
15 300 -0.0013      -3 -4              $ Var reduction cell
16 300 -0.0013      -3 -5 4            $   "                    "
17 300 -0.0013      -3 -6 5            $   "                    "
18 300 -0.0013      -3 -7 6            $   "                    "
19 300 -0.0013      -3  1 7            $   "                    "
20 200 -19.3        -1 -2              $ Gold
30 100 -2.33        -1  2              $ Si
40 0                 3                 $ Void

c Surface cards
1 rcc  0 0 0   0 0 0.0051   0.5
2 pz    0.0001
3 rpp  -0.6 0.6   -0.6 0.6   -0.15 0.006
4 pz    -0.12
5 pz    -0.09
6 pz    -0.06
7 pz    -0.03

c data cards
nps 10000000
imp:p 1 2.06m 1.05m 1.05m 0.595m 2.04m 1.15m 0
imp:e 1    1    1    1     1     1     1 0
mode p e
phys:p  100 1 0 0 0
c - - - Materials - - - - - - - - - - - - - - - - - - - - -
m100    14000.04p       -1.0              $Si
m200    79000.04p       -1.0              $Au
m300     7000.04p -0.755636              $Air
         8000.04p -0.231475
        18000.04p -0.012889
c - - - Source - - - - -Ba-133 - - - - - - - - - - - - -
sdef pos=0 0 -0.14  par=2 erg=d1
```

59

```
SI1 L   0.00429 0.030625 0.030973 0.08   0.302851 0.356
SP1 D   0.163    0.351     0.643     0.341 0.1833    0.6205
c - - - Tallies - - - - - - - - - - - - - - - - - - - - - - - -
f8:p 30
fmesh4*:p    geom=xyz    origin=-0.6 -0.6 -0.15
             imesh=0.6    iints=100
             jmesh=0.6    jints=100
             kmesh=0.006  kints=50
             factor=5e18
FT8 GEB 0 0.02 0
e8 0 1e-5 1000ilog 0.4
```

References

1. Chen, H., S. A. Awadalla, P. Marthandam, K. Iniewski, P. H. Lu, and G. Bindley. 2009. *CZT Device with Improved Sensitivity for Medical Imaging and Homeland Security Applications*. SPIE-2009 Invited Talk (Paper 7449-1).

2. Berger, M. J., J. H. Hubbell, S. M. Seltzer, J. Chang, J. S. Coursey, R. Sukumar, D. S. Zucker, and K. Olsen. 2001. XCOM: Photon Cross Sections Database, NIST Standard Reference Database 8 (XGAM).

3. Luke, P. N., and M. Amman. 2006. *Room-Temperature Replacement for Ge Detectors – Are We There Yet?* IEEE Nuclear Science Symposium Conference Record.

4. Furukawa, A. and S. Ideshita. 1994. *Origin of Deep Donors in AlSb Grown by Molecular Beam Epitaxy*. J. Appl. Phy. 75, 5012.

5. Ayers, J. E. 2007. *Heteroepitaxy of Semiconductors; Theory, Growth and Characterization*. CRC Press Taylor and Francis Group.

6. MCNP – A General Monte Carlo N-Particle Transport, Version 5, Volume II: User's Guide, Rev. Feb 2008.

7. MCNP – A General Monte Carlo N-Particle Transport, Version 5, Volume I: Overview and Theory, Rev. Feb 2008.

8. Knoll, G. F. 2010. *Radiation Detection and Measurement: Fourth Edition*, John Wiley & Sons, Inc.

9. Swierkowski, S. P. and G. A. Armantrout. 1975. *Prognosis for High-Z Semiconductor Detectors*. IEEE Transactions on Nuclear Science, Vol NS-22.

10. Swierkowski, S. P. 1976. *A Comprehensive Model for Predicting Semiconductor Detector Performance*. IEEE Transactions of Nuclear Science, Vol. NS-23, No.1.

11. Witt, A. F. et al. 1994. *Top-Seed Solution Growth and Characterization of AlSb Single Crystals for Gamma-Ray Detectors* DoE Grant# DE-FG08-94NV11627.

12. Ortec, *Overview of Semiconductor Photon Detectors*. www.ortec-online.com, 2010.

13. Balakrishnan, G., S. Huang, L. R. Dawson, Y.-C. Xin, P. Conlin, and D. L. Huffaker. 2005. *Growth Mechanisms of Highly Mismatched AlSb on a Si Substrate*. App. Phy. Lett. 86, 034105.

14. Wald, F. V., J. Bullitt and R. O. Bell. 1975. *Bi(2)S(3) as a Hgh Z Material for Gamma-Ray Detectors.* IEEE Transactions on Nuclear Science, Vol. NS-22.

15. Aberg, D., P. Erhart, A. J. Williamson, and V. Lordi. 2008. *Instrinsic Point Defects in Aluminum Antimonide*. Phys. Rev. B 77, 165206.

16. Lordi, V., D. Aberg, P. Erhart, and K. J. Wu. 2007. *First Principles Calculation of Point Defects and Mobility Degradation in Bulk AlSb for Radiation Detection Application.* Hard X-Ray and Gamma-Ray Detector Physics VIII, San Diego, CA.

17. Pani, R., R. F. Laitano, and R. Pellegrini. 1987. *Diagnostic X-Ray Spectra Measurements Using a Silicon Surface Barrier Detector*. Phys. Med. Biol., Vol. 32, No 9, 1135-1149.

18. Kaganer, V. M., R. Kohler, M. Schmidbauer, and R. Opitz. 1997-I. *X-Ray Diffraction Peaks Due to Misfit Dislocations in Heteroepitaxial Structures.* Phys. Rev. B, Vol. 55, No. 3.

19. Ottoviani, G., C. Canali, and A. Alberigi Quaranta. 1975. *Charge Carrier Transport Properties of Semiconductor Materials Suitable for Nuclear Radiation Detectors*. IEEE Transactions on Nuclear Science, Vol. NS-22.

20. Bennett, B. R., W. J. Moore, M. J. Yang, and B. V. Shanabrook. 2000. *Transport Properties of Be- and Si-doped AlSb*. J. Appl. Phys., Vol. 87, No. 11.

21. Brar, B. and D. Leonard. 1995. *Spiral Growth of GaSb on (001) GaAs using Molecular Beam Epitaxy.* Appl. Phys. Lett. 66, 463.

22. Kutny, V. E., A. V. Rybka, A. S. Abyzov, L. N. Davydov, V. K. Komar, M. S. Rowland, and C. F. Smith. 2001. *AlSb Single-Crystal Grown by HPBM*. Nuclear Instruments and Methods in Physics Research A 458, 448-454.

23. Du, M.-H. 2009. *Defects in AlSb: A Density Functional Study*. Phys. Rev. B 79, 045207.

24. Armantrout, G. A., S. P. Swierkowski, J. W. Sherohman, and J. H. Yee. 1977. *What Can Be Expected From High-Z Semiconductor Detectors?* IEEE Transactions on Nuclear Science, Vol. NS-24, No. 1.

25. Yee, J. H., S. P. Swierkowski, and J. W. Sherohman. 1977. *AlSb as a High-Energy Photon Detector*. IEEE Transactions on Nuclear Science, Vol. NS-24, No. 4.

26. Chang, C., H. Takaoka, L. L. Chang, and L. Esaki. 1982. *Molecular Beam Epitaxy of AlSb*. Appl. Phys. Lett. 40(11).

27. Jallipalli, A., G. Balakrishnan, S. H. Huang, T. J. Rotter, K. Nunna, B. L. Liang, L. R. Dawson, and D. L. Huffaker. 2009. *Structural Analysis of Highly Relaxed GaSb Grown on GaAs Substrates with Periodic Interfacial Array of 90˚ Misfit Dislocations*. Nanoscale Research Letters.

28. Smith, H. A. and M. Lucas. 1991. *Passive Nondestructive Assay of Nuclear Materials: Chapter 3; Gamma Ray Detectors*. Office of Nuclear Regulatory Research, Washington DC.

29. Bertolini, G. and A. Coche. 1968. *Semiconductor Detectors*. North-Hollland, Amsterdam.

30. Haller, E. E., H. W. Kraner, and W. A. Higinbotham. 1982. *Nuclear Radiation Detector Materials*. Materials Research Society Symposia Proceedings, Vol. 16, Boston, Mass.

31. Alexiev, D., D. A. Prokopovich, S. Thomson, L. Mo, A. B. Rosenfield and M. Reinhard. *A Review of Liquid Phase Epitaxial Grown Gallium Arsenide.*

32. Gu, Y., J. P. Romankiewicz, J. K. David, J. L. Lensch, and L. J. Lauhon. 2006. *Quantitative Measurement of the Electron and Hole Mobility-Lifetime Products in Semiconductor Nanowires*. Nano Letters, Vol. 6, No. 5, 948-952.

33. He, Z. 2001. *Review of the Schockley-Ramo Theorem and its Application in Semiconductor Gamma-Ray Detectors*. Nuclear Inst. and Methods A 463, 250-267.

34. Jallipalli, A., G. Balakrishnan, S. Huang, T. Rotter, K. Nunna, B. Liang, L. Dawson, D. Huffaker. 2009. *Structural Analysis of Highly Relaxed GaSb Grown on GaAs Substrates with Periodic Interfacial Array of 90° Misfit Dislocations*. Nanoscale Res Lett.

35. van der Pauw, L. J. 1958. *A Method of Measuring the Resistivity and Hall Coefficient on Lamellae of Arbitrary Shape*. Philips Technical Review, Vol.20, No.8.

36. Thurber, W. R. *Semiconductor and Dimensional Metrology Division: The Hall Effect*. NIST, www.nist.gov/pml/div683/hall_effect.cfm.

37. Gruhn, C. R. 1977. *Epitaxial Silicon Semiconductor Detectors: Past Developments, Future Prospects, IEEE Transactions on Nuclear Science*. Vol. NS-24, No. 1.

38. Fiederle, M., A. Fauler, J. Konrath, V. Babentsov, J. Franc, and R. B. James. 2004. *Comparison of Undoped and Doped High Resitivity CdTe and (Cd,Zn)Te Detector Crystals*. IEEE Transactions on Nuclear Science, Vol. 51, No. 4.

39. Butler, J. F., C. L. Lingren and F. P. Doty. 1992. *Cd$_{1-x}$Zn$_x$Te Gamma Ray Detectors*. IEEE Transactions on Nuclear Science, Vol. 39, No. 4.

40. Klema, E. D. 1964. *Preparation of High-Resistivity Silicon Surface-Barrier Detectors for use at Large Reverse Bias Voltages*. Nuclear Instruments and Methods, Vol. 26, 205-208.

41. Hartmann, F. 2009. *Evolution of Silicon Sensor Technology in Particle Physics.* STMP 231 (Springer, Berlin Heidelberg), DOI 10.1007/978-3-540-44774-0.

42. Simpson, R. E. 1987. *Introductory Electronics for Scientists and Engineers, 2nd Ed.* Allyn and Bacon.

43. Hyperphysics.phy-astr.gsu.edu/hbase/solids/Fermi.html#c2

44. Titus, A. H., Maurice C-K. Cheung and Vamsy P. Chodavarapu. 2011. *CMOS Photodetectors*, Photodiodes - World Activities in 2011, Prof. Jeong Woo Park (Ed.), ISBN: 978-953-307-530-3, InTech, DOI: 10.5772/20194.

45. Neamen, D. A. 2003. *Semiconductor Physics and Devices: Basic Principles, 3rd Ed.* McGraw-Hill.